AGU PUBLICATIONS

JGR

Journal of Geophysical Research: Solid Earth

RESEARCH ARTICLE
10.1002/2017JB013971

Key Points:
- We apply a new spectral decomposition method to examine earthquake source scaling
- The data are consistent with an increase in average Brune-type stress drop with seismic moment
- The inferred deviation from self-similarity is model dependent and trades off with the assumed high-frequency falloff rate

Supporting Information:
- Supporting Information S1
- Data Set S1
- Data Set S2
- Data Set S3
- Data Set S4
- Data Set S5

Correspondence to:
D. T. Trugman,
dtrugman@ucsd.edu

Citation:
Trugman, D. T., and P. M. Shearer (2017), Application of an improved spectral decomposition method to examine earthquake source scaling in Southern California, *J. Geophys. Res. Solid Earth*, *122*, doi:10.1002/2017JB013971.

Received 10 JAN 2017
Accepted 19 MAR 2017
Accepted article online 23 MAR 2017

Application of an improved spectral decomposition method to examine earthquake source scaling in Southern California

Daniel T. Trugman[1] **and Peter M. Shearer**[1]

[1] Institute of Geophysics and Planetary Physics, Scripps Institution of Oceanography, La Jolla, California, USA

Abstract Earthquake source spectra contain fundamental information about the dynamics of earthquake rupture. However, the inherent tradeoffs in separating source and path effects, when combined with limitations in recorded signal bandwidth, make it challenging to obtain reliable source spectral estimates for large earthquake data sets. We present here a stable and statistically robust spectral decomposition method that iteratively partitions the observed waveform spectra into source, receiver, and path terms. Unlike previous methods of its kind, our new approach provides formal uncertainty estimates and does not assume self-similar scaling in earthquake source properties. Its computational efficiency allows us to examine large data sets (tens of thousands of earthquakes) that would be impractical to analyze using standard empirical Green's function-based approaches. We apply the spectral decomposition technique to *P* wave spectra from five areas of active contemporary seismicity in Southern California: the Yuha Desert, the San Jacinto Fault, and the Big Bear, Landers, and Hector Mine regions of the Mojave Desert. We show that the source spectra are generally consistent with an increase in median Brune-type stress drop with seismic moment but that this observed deviation from self-similar scaling is both model dependent and varies in strength from region to region. We also present evidence for significant variations in median stress drop and stress drop variability on regional and local length scales. These results both contribute to our current understanding of earthquake source physics and have practical implications for the next generation of ground motion prediction assessments.

Plain Language Summary Just as a line of music can be characterized in terms of its amplitude and pitch, earthquakes can be characterized in terms of their magnitude and frequency content. The frequency content of an earthquake depends on its size, with smaller earthquakes having systematically higher "pitches" than larger ones. Previous studies in earthquake seismology have assumed that the frequency content of earthquakes exhibits a particularly simple form of scaling with earthquake size known as self-similarity. Under this paradigm, large earthquakes are perfectly scaled-up versions of small ones, with the physical properties of the earthquake scaling in much the same way as font size does on a computer. In this article, the authors develop a new method to examine the frequency content of tens of thousands of earthquakes occurring in different regions of Southern California over the past 15 years. The authors find that the frequency content of these earthquakes deviated significantly from the self-similar model, with larger earthquakes being enriched in more high-frequency energy than expected. This result has important implications for earthquake hazard, as the most damaging ground motions are generated by the high-frequency seismic waves of the largest earthquakes.

1. Introduction

Analyses of waveforms recorded by arrays of seismic stations provide the most fundamental observational constraints on earthquake occurrence. While the arrival times of different phases of seismic energy are routinely used to determine the hypocentral location, the detailed features of the spectra of recorded waveforms give a snapshot of the earthquake source and can yield insight into the complex physical processes underlying earthquake nucleation, rupture, and arrest. Of particular interest is the earthquake source spectrum, the frequency-domain analog of the moment-rate (or source-time) function that describes the temporal evolution of slip on the fault interface. The amplitude and shape of source spectra can be used to infer key earthquake source parameters like seismic moment, radiated energy, and stress drop that are essential for seismic hazard assessment.

The waveform spectrum recorded by a seismometer is a convolution of source, path, and receiver terms. To isolate source spectra, one must somehow correct for these effects. There exist a number of established approaches for attempting to do so, including empirical Green's function methods tailored for detailed study of individual earthquakes [e.g., *Mori and Frankel*, 1990; *Hough*, 1997; *Prieto et al.*, 2006; *Abercrombie*, 2013; *Huang et al.*, 2016], and larger-scale stacking and generalized inversion approaches [e.g., *Castro et al.*, 1990; *Shearer et al.*, 2006; *Oth et al.*, 2011] that are more readily applicable to larger data sets of earthquakes. While each technique has its own strengths, none can perfectly resolve the contribution of the earthquake source to the observed waveform spectra, even in idealized scenarios. This tradeoff between source and path effects, when combined with noise and the limited signal bandwidth of raw waveform data, implies that earthquake source parameter estimates, while critical to our understanding of earthquake hazard, are subject to considerable uncertainty [e.g., *Hough*, 1996; *Prieto et al.*, 2007; *Abercrombie*, 2015; *Kane et al.*, 2011; *Cotton et al.*, 2013]. Thus, any technique designed to study earthquake source spectra and source parameters should include realistic uncertainty estimates.

Here we describe a spectral decomposition technique that is capable of providing reliable source spectral estimates for large ensembles of earthquakes. The method builds upon the basic approach used by *Shearer et al.* [2006] to analyze *P* wave spectra of more than 60,000 M_L 1.5–3.1 earthquakes occurring in Southern California from 1989 to 2001. The technique uses an iterative, robust least squares algorithm to partition the observed spectra into source, station, and traveltime (path) terms, with L1-norm weights applied to large misfit residuals to mitigate the influence of the outliers pervasive in seismic data sets. We develop a nonparametric resampling approach to estimate source parameter uncertainties and apply an automated algorithm to detect and discard clipped waveforms that are common for larger events.

A crucial improvement of our new technique over that of *Shearer et al.* [2006] is that our approach does not presume the self-similar scaling of earthquake source properties first proposed by *Aki* [1967], in which stress drop is constant with moment. While self-similarity is intuitively appealing and has been supported in many studies [e.g., *Choy and Boatwright*, 1995; *Ide and Beroza*, 2001; *Ide*, 2003; *Prieto et al.*, 2004; *Allmann and Shearer*, 2009; *Baltay et al.*, 2010, 2011; *Abercrombie et al.*, 2017], other studies have found evidence for a slight increase in stress drop or scaled energy with moment [e.g., *Mayeda and Walter*, 1996; *Izutani and Kanamori*, 2001; *Mori et al.*, 2003; *Mayeda et al.*, 2005; *Takahashi et al.*, 2005; *Mayeda et al.*, 2007; *Calderoni et al.*, 2013; *Pacor et al.*, 2016a; *Lin et al.*, 2016; *Poli and Prieto*, 2016]. This controversy over self-similarity has important theoretical implications for our understanding of the scale dependence of earthquake rupture processes [*Kanamori and Rivera*, 2004; *Abercrombie and Rice*, 2005; *Walter et al.*, 2006; *Cocco et al.*, 2016], as well as practical ramifications for hazard analyses [e.g., *Field et al.*, 2014; *Yenier and Atkinson*, 2015; *Petersen et al.*, 2016] that implicitly assume self-similar scaling.

We apply the improved spectral decomposition technique to revisit the question of earthquake scaling in Southern California. We analyze source parameters and their scaling with moment for more than 10,000 **M**1 to **M**5 earthquakes in five regions of recent seismic activity (Figure 1) recorded by the modern (2002–2016) Southern California Seismic Network (SCSN) [*Hutton et al.*, 2010]: (1) the Yuha Desert, including thousands of aftershocks of the 2010 M_w 7.2 El Mayor-Cucapah earthquake; (2) the trifurcation zone of the San Jacinto Fault, in which the recent 2016 M_w 5.2 Borrego Springs earthquake was located; (3) the Big Bear region on the western boundary of the Mojave Desert; and the rupture zones of the prominent (4) 1992 M_w 7.3 Landers and (5) 1999 M_w 7.1 Hector Mine earthquakes. We present evidence for an increase in median stress drop with moment for these regions and also demonstrate that the observed deviation from self-similarity is sensitive to modeling assumptions and in particular on the assumed high-frequency falloff rate. We further show that there are significant regional and local variations in median stress drop, stress drop variability, and source parameter scaling. This study outlines the computational framework for future studies to extend these preliminary findings to larger regions to obtain a updated catalog of source parameter estimates [*Shearer et al.*, 2006] that would provide key constraints on earthquake source physics and inform the next generation of ground motion prediction equations in Southern California and worldwide.

2. Data and Methods

Our spectral decomposition technique to analyze earthquake source spectra has four main steps: (1) computation of *P* wave spectra from the vertical-component waveform time series records of each earthquake; (2) application of an iterative, robust least squares inversion procedure to decompose the observed (data)

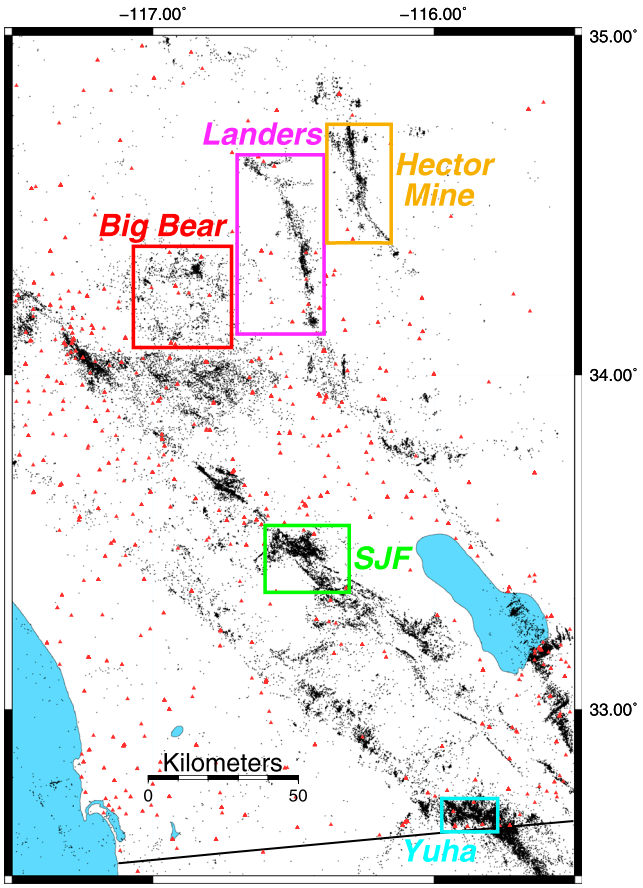

Figure 1. Map view of Southern California seismicity, showing geographic bounds for the five study regions—Yuha Desert (Yuha), San Jacinto Fault Trifurcation Zone (SJF), Big Bear, Landers, and Hector Mine—considered in this study. Seismicity (black dots) is derived from the relocated catalog of [*Hauksson et al.*, 2012], with only $M_L \geq 1.1$ events occurring from January 2002 through September 2016 shown (consistent with the magnitude range and time period of this study). Vertical-component stations from the Southern California Seismic Network are marked (red triangles) for reference.

spectra into event, station, and traveltime terms; (3) stacking of relative event spectra in bins of spectral moment to estimate an empirical correction (or empirical Green's function, EGF) for average near-source attenuation and other path effects common to all events; and (4) estimation of corner frequency, seismic moment, and stress drop for individual events, with estimates of parameter uncertainties obtained using a nonparametric resampling method. Steps (1) and (2) are largely the same as the method described by *Shearer et al.* [2006], with minor modifications designed to improve the algorithm's robustness and capability of processing data sets over a wider magnitude range than the M_L 1.5–3.1 considered for their study. Steps (3) and (4), while conceptually similar, contain major modifications and improvements that allow for a more rigorous examination of self-similarity.

2.1. Waveform Data and Spectral Computation

We use the Seismic Transfer Protocol (STP) tool of the Southern California Earthquake Data Center (SCEDC, http://scedc.caltech.edu/, last accessed 4 December 2016) to obtain raw waveform data and phase pick information from M_L 1.1 and greater events occurring during the time period from January 2002 through September 2016 within the five regions listed in Figure 1. For each event, we consider waveforms from vertical-component, short-period, and high-broadband channels (EHZ or HHZ) on stations within 80 km. Most such records have 100 Hz sampling frequencies, and we exclude all records with a lower sampling rate while subsampling any 200 Hz records to 100 Hz to maximize data availability.

For each event, we select a magnitude-dependent window length for spectral computations ranging from 1.5 to 4.5 s, with longer windows used for events of higher magnitude to ensure adequate resolution of the

spectral corner frequency [*Ross and Ben-Zion*, 2016; *Abercrombie et al.*, 2017]. We define the signal window to begin 0.05 s before the cataloged *P* arrival to account for potential errors in the pick time and define a noise window of equal length (used for signal-to-noise computations) immediately preceding the signal window. Clipped waveforms are common for near-source stations recording $\mathbf{M} \geq 3$ events [*Shearer et al.*, 2006; *Yang and Ben-Zion*, 2010], and we detect and exclude all waveforms flagged as clipped using a classification algorithm that compares the probability distribution of observed waveform amplitudes to that of known, clipped waveforms. For the nonclipped waveforms, we then compute velocity amplitude spectra for the signal and noise windows using a multitaper algorithm [*Park et al.*, 1987; *Prieto et al.*, 2009]. We convert these velocity spectra to displacement, resample all spectra to the frequency points corresponding to the shortest time windows (1.5 s, which have the coarsest frequency sampling), and only further consider spectra with average signal-to-noise amplitude greater than 5 in each of five frequency bands (2.5–6, 6–10, 10–15, 15–20, and 20–25 Hz). Note that these are somewhat more stringent quality control criteria than those used by *Shearer et al.* [2006], who used a fixed spectral window length, tested signal-to-noise from 5 to 20Hz, and did not explicitly check for clipped waveforms. We implemented the above preprocessing steps and selection criteria to ensure that we could reliably assess source scaling over a wide range of event magnitudes (both smaller and larger). The *P* wave spectra meeting these quality control criteria comprise the input data to the spectral decomposition inversion technique described below.

2.2. Spectral Decomposition and Relative Source Spectra

The observed displacement spectra are a convolution of source, path, and station effects, the latter of which includes both site effects and the instrument response. In the frequency domain, the recorded spectra $d(f)$ can thus be written as a product of event (source), path, and station spectra:

$$d(f) = e(f)\, p(f)\, \mathrm{st}(f), \tag{1}$$

which can be linearized by working in the log f domain,

$$\log d(f) = \log e(f) + \log p(f) + \log \mathrm{st}(f). \tag{2}$$

The basic idea behind the spectral decomposition technique is that because each earthquake will be recorded by many stations, each station will record many earthquakes, and each approximate source-receiver path will be traversed many times, it should be possible to solve for each contribution as part of an overdetermined system of equations defined by the input data spectra.

More precisely, consider the observed displacement spectra d_{ij} corresponding to event i, recorded by station j. Approximating the path term p_{ij} as a traveltime-dependent term $\mathrm{tt}_{k(i,j)}$ that depends primarily on the distance from the source to the station, we can write a linear equation of the form

$$d_{ij} = e_i + \mathrm{tt}_{k(i,j)} + \mathrm{st}_j + r_{ij}, \tag{3}$$

for each observed spectra, where r_{ij} is a residual error term. Equation (3) defines an overdetermined inverse problem in which the number of observations (recorded spectra, d) outnumber the desired model parameters e, tt, st. We discretize the traveltime terms (indexed by k) in bins of 1 s of observed source-receiver traveltime and only further consider spectra from events that are observed by at least five stations, and stations that observe at least 20 events.

For stability and to mitigate the influence of data outliers, we use an iterative, robust least squares method to solve sequentially for model parameters tt_k, st_j, and e_i, where L1-norm weights are applied to large misfit residuals at each iteration. The inversion is performed independently for each frequency point. The focus of this study is on the source terms e_i, so the traveltime and station terms tt_k and st_j are essentially nuisance parameters but do contain useful information about midcrustal attenuation and site effects [e.g., *Castro et al.*, 1990; *Shearer et al.*, 2006; *Oth et al.*, 2011] that may be of interest for ground motion and seismic hazard analyses. Note that strong near-surface attenuation and its lateral variability will largely be absorbed into the station (site) terms and the empirical Green's function correction described below.

2.3. Spectral Stacking and EGF-Corrected Source Spectra

One limitation of the above spectral decomposition is that it can only resolve relative differences between the source spectra of each event. Thus, it is necessary to further correct for propagation effects that are common to

all paths (e.g., near-source attenuation and common site or instrument effects) in order to interpret the source spectra within the framework of theoretical earthquake source models. *Shearer et al.* [2006] resolved this ambiguity by first computing averaged, stacked spectra in bins corresponding to a range of spectral moments (i.e., long-period spectral amplitudes). They then solved for the correction term (i.e., the empirical Green's function or EGF) that minimized the root-mean-square (RMS) misfit between the EGF-corrected stacked spectra, and a Brune-type [*Brune*, 1970] circular crack source model of the form

$$u(f) = \frac{\Omega_0}{1 + (f/f_c)^n}, \tag{4}$$

where Ω_0, f_c, and n are the spectral moment (proportional to seismic moment, M_0), corner frequency, and high-frequency falloff rate, respectively. For simplicity, *Shearer et al.* [2006] fixed $n = 2$ (as in the canonical ω^{-2} model) and assumed that the stacked spectra were well described by a self-similar, constant stress drop model in which stress drop $\Delta\sigma$ is related to corner frequency and seismic moment by

$$\Delta\sigma = \frac{7}{16} M_0 \left(\frac{f_c}{k\beta} \right)^3 \tag{5}$$

for shear wave speed β and a constant k (here 0.32 following *Madariaga* [1976], derived for a circular crack with constant stress drop, elliptical slip, and a constant rupture velocity $v_r = 0.9\beta$). *Shearer et al.* [2006] performed a grid search over trial values of stress drop $\Delta\sigma$ and determined the EGF correction from the average residual (across all stacks) between the observed and theoretical Brune-type spectra (equation (4)), given $\Delta\sigma$ and the relative moment of each stack. They showed that the resulting EGF and self-similar Brune model produced a reasonable overall fit to the moment-binned spectral stacks averaged over their entire data set of ~60,000 earthquakes and proceeded to show that median stress drops estimated for individual events using this EGF were nearly constant with moment. However, this approach may have biased the results toward self-similarity because it did not test whether non-self-similar models could produce equal or even better fits to the data.

Here we generalize the stacking approach [*Shearer et al.*, 2006] used to obtain the EGF, while relaxing the assumption of self-similar scaling between the stacked spectra. Following *Shearer et al.* [2006], we stack source spectra in bins of spectral moment, Ω_0. Each of the stacked spectra thus represents the average relative source spectra of events with comparable seismic moment M_0 (which is proportional to Ω_0). Note that we define Ω_0 using the mean amplitude over the 2.5–4 Hz band, as the signal-to-noise worsens at lower frequencies.

Rather than assume a constant stress drop $\Delta\sigma$ for each stack, we allow for the possibility of a variation in mean stress drop with moment by comparing generalized linear models of the form $\log_{10} \Delta\sigma\,(\Omega_0|\epsilon) = \epsilon_0 + \epsilon_1\,\Omega_0 + \epsilon_2\,\Omega_0^2 +, \ldots, +\epsilon_m\,\Omega_0^m$, where $\epsilon = [\epsilon_0, \epsilon_1, \epsilon_2, \ldots, \epsilon_m]$ is a model vector whose parameters specify a degree-m polynomial-type scaling of stress drop and moment (both measured in logarithmic units). The degree-0 model corresponds to a constant stress drop model that is functionally equivalent to the approach used by *Shearer et al.* [2006]. The results presented in this study compare the self-similar (degree-0) parameterization to models with linear (degree-1) scaling [e.g., *Kanamori and Rivera*, 2004; *Mayeda et al.*, 2007; *Oth*, 2013]:

$$\log_{10} \Delta\sigma\,(\Omega_0|\epsilon) = \epsilon_0 + \epsilon_1\,\Omega_0. \tag{6}$$

We also tested higher-order models, as well as those with unconstrained variation of stress drop with moment, but found the marginal improvement in data misfit provided by such models to be insufficient to warrant the increase in model complexity [*Akaike*, 1974] and tendency for instability (symptomatic of overfitting noise in the stacked spectra). The basic steps in our new, iterative algorithm can be summarized as follows (see Figure 2 for a representative example using data from the Yuha Desert region):

1. Bin events by spectral moment Ω_0 and compute stacked source spectra for each bin, requiring at least 20 events per bin to ensure the stacked spectra are well resolved.
2. Initialize the parameter vector $\epsilon_i = [0, 0]$ to a starting value implying constant stress drop for each bin (here the subscript i denotes the current iteration of the optimization algorithm).
3. Compute theoretical source spectra for each stack, given its stress drop value defined by the current parameter vector ϵ_i and mean spectral moment Ω_0 (proportional to M_0).
4. Estimate the EGF correction from the residual between the observed and theoretical stacked spectra, at all frequency points, averaged across all stacks. Note that while each stack has its own unique stress drop value, the EGF correction is common to all of the stacked spectra.

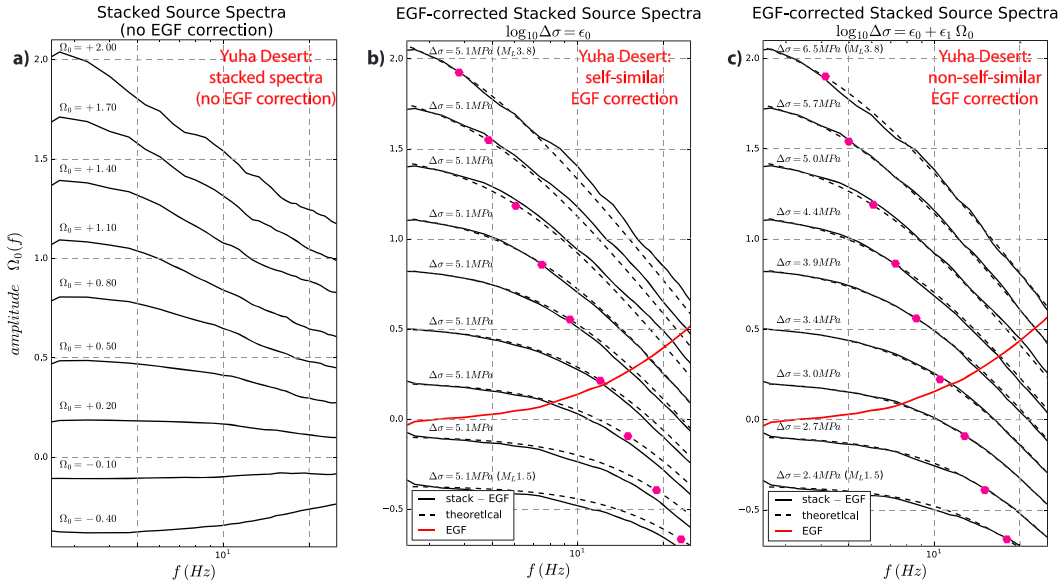

Figure 2. Example of stacked source spectra from the Yuha Desert region, before and after the EGF correction for common path effects (see text for details). (a) Stacked source spectra (binned by spectral moment Ω_0), prior to the EGF correction. (b) EGF-corrected source spectra (solid black lines), assuming a self-similar, constant stress drop source model with f^{-2} falloff at high frequencies. Theoretical source spectra corresponding to each stack are shown with dashed black lines, with the implied corner frequency of the fit marked for reference. The self-similar model fits poorly for both lower and higher values of Ω_0. (c) EGF-corrected source spectra (solid black lines), assuming a source model in which stress drop increases linearly with moment (both measured in logarithmic units). Theoretical source spectra corresponding to each stack are shown with dashed black lines, with the implied corner frequency of the fit marked for reference. This model provides a significantly better fit than the self-similar model.

5. Compute the weighted RMS misfit between the EGF-corrected, observed spectra and the theoretical spectra in the frequency band from 2.5 to 25 Hz. Here we apply weights inversely proportional to log *f* to prevent random fluctuations in the high-frequency portion of the spectra from dominating the fit.
6. Update $\epsilon_i \rightarrow \epsilon_{i+1}$ using a conjugate gradient algorithm and repeat steps 3–6 until convergence to the minimum of the misfit function. Note that while first-order models can be solved in analogous ways using a grid search over the model parameters, the iterative conjugate gradient approach provides a unified computational framework for efficiently comparing higher-order or otherwise more complex models.

The final EGF obtained at the convergence point is used to correct the shape of the relative source spectra of each individual event for propagation effects that are common to all paths, making them directly comparable to the theoretical source model of interest (Figures 2 and 3). For the main results presented in this paper, we assume the widely used *Brune* [1970] source model with ω^{-2} spectral falloff (equation (4) with $n = 2$) but discuss in detail the influence of this choice in section 4.

The use of stacked spectra in the EGF estimation procedure has certain advantages, most notably, that it relies solely on the relative shape of well-constrained, averaged spectra within the high signal-to-noise band, and not on resolving the corner frequencies of smaller individual events, some of which may be beyond the usable signal bandwidth. However, it does neglect the lateral and depth-dependent variations in average attenuation properties that are not accounted for in the station terms, which may be important for studies over larger length scales than within the five regions we consider here. In these cases, nearest neighbor or spatial interpolation techniques could be incorporated into the stacking procedure in order to include lateral and depth-dependent attenuation corrections into the spectral decomposition algorithm [e.g., *Shearer et al.*, 2006].

2.4. Source Parameter Estimates: Corner Frequency, Moment, and Stress Drop

With the EGF-corrected source spectra in hand, we are now able to estimate source parameters for each event. To compute stress drop $\Delta\sigma$ as defined by (5), we need estimates of corner frequency f_c, seismic moment M_0,

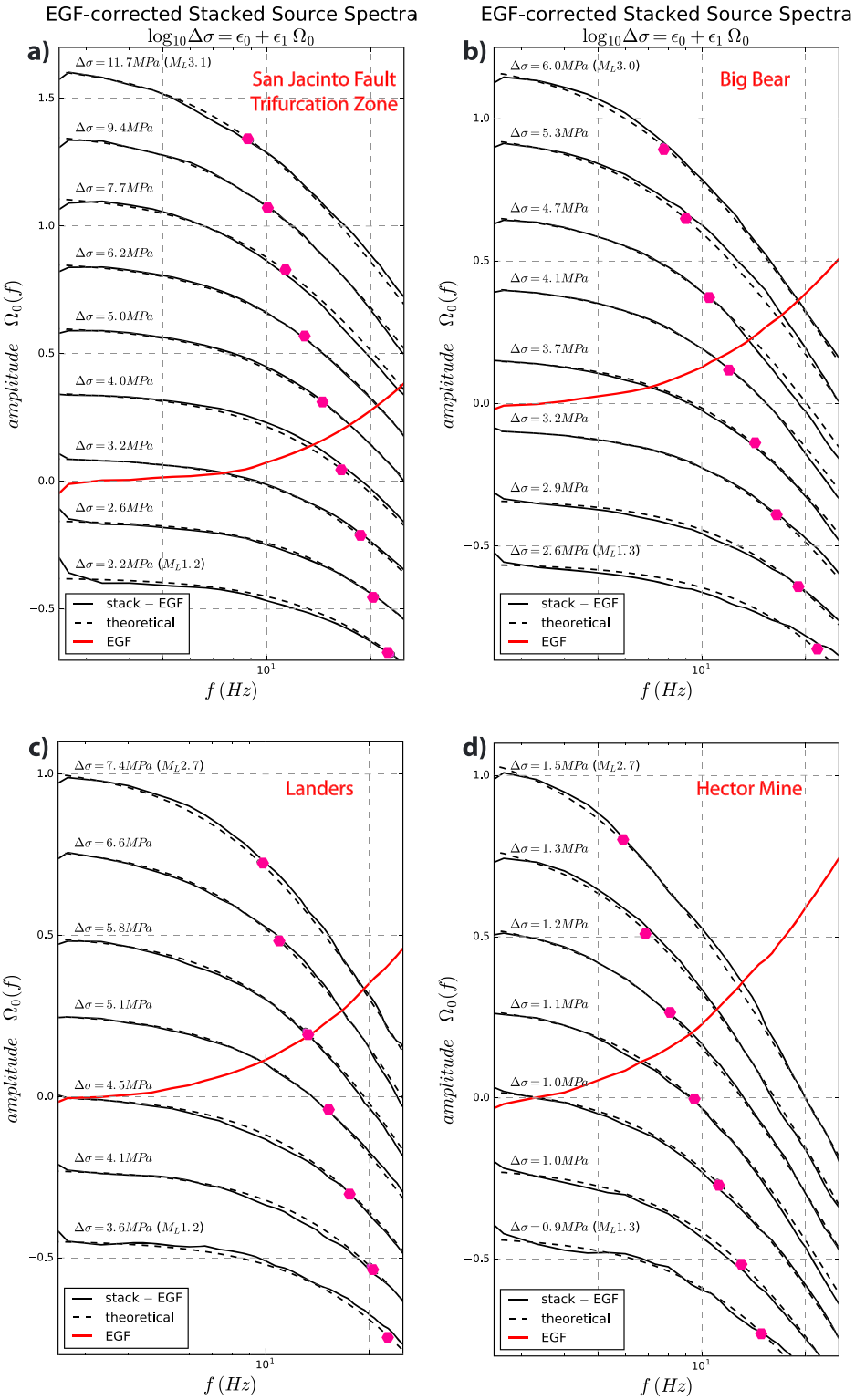

Figure 3. EGF-corrected, stacked source spectra from the (a) San Jacinto Fault Trifurcation Zone, (b) Big Bear, (c) Landers, and (d) Hector Mine regions. Each EGF-corrected source spectra (solid black lines, binned by spectral moment Ω_0) assumes a source model in which stress drop increases with moment (as in Figure 2c for the Yuha region). Theoretical source spectra corresponding to each stack are shown with dashed black lines, with the implied corner frequency of the fit marked for reference.

and shear wave velocity β. We first estimate the corner frequency f_c using a bounded optimization algorithm that minimizes the weighted RMS residual between the observed, EGF-corrected source spectra $s_i(f)$ and theoretical spectra $\hat{s}_i(f|f_c)$ in the 2.5–25 Hz band (where again, inverse log f weights are applied to prevent the high-frequency portion of the spectra from dominating the fit).

Although some of the larger events ($M_L \geq 3.5$) have independent estimates of M_0 from regional analyses of long-period waveforms, the vast majority of the events we consider are listed by local magnitude M_L rather than moment magnitude M_w. We therefore need a self-consistent way of computing M_0 for all events, large and small, as numerous studies [e.g., *Hutton et al.*, 2010; *Ross et al.*, 2016; *Munafò et al.*, 2016] have demonstrated that $M_w \neq M_L$ for smaller events. We follow the same basic approach used by *Shearer et al.* [2006] and assume the M_0 is proportional to the spectral moment Ω_0, but apply a correction term to the Ω_0 estimates obtained from the 2.5–4 Hz band (section 2.3) to zero frequency using the observed corner frequency f_c (this correction is more important for the larger events with $f_c < 4$ Hz, where the spectral decay significantly reduces the observed 2.5–4 Hz amplitude). We derive the proportionality constant between M_0 and Ω_0 in two steps [*Shearer et al.*, 2006]. We first perform regression analysis to calibrate a linear relationship between M_L and Ω_0: $\hat{M}_L = a_0 + a_1 \Omega_0$. The amplitude-adjusted local magnitudes $\hat{M}_L$ are then converted to moment magnitudes M_w and absolute moment M_0 by assuming that $M_w \approx \hat{M}_L$ at $\mathbf{M} = 3.50$ for earthquakes within Southern California [*Hutton et al.*, 2010; *Ross et al.*, 2016]. This regression analysis is performed separately for each region, as the regression coefficients depend slightly on local attenuation.

Finally, we use a smoothed version of the 1-D velocity model of *Hadley and Kanamori* [1977] and the waveform-relocated event depths from the catalog of *Hauksson et al.* [2012] to compute depth-dependent shear wave velocities β for all events and use our estimates of f_c, M_0, and β to compute stress drop $\Delta\sigma$ for each event (equation (5)). We use the revised P wave value of the constant $k = 0.38$ from the numerical study of *Kaneko and Shearer* [2014], though encourage caution in interpreting the absolute values of the stress drop estimates, which can be highly model dependent. More robust are the relative variations in stress drop estimated using a uniform and consistent set of modeling assumptions and processing procedures.

2.5. Source Parameter Uncertainties: Corner Frequency, Moment, and Stress Drop

Each source spectra estimate is in some sense an average over all stations recording the event, and we utilize this fact in order to characterize the parameter uncertainties associated with our f_c estimates. To do so, we first define the apparent source spectra $\tilde{s}_{ij}$ [e.g., *Pacor et al.*, 2016b] for each station j recording event i:

$$\tilde{s}_{ij} = d_{ij} - \mathrm{tt}_{k(i,j)} - \mathrm{st}_j - \bar{r}_{ij} - \mathrm{EGF}_{\mathrm{corr}}, \tag{7}$$

where d, tt, st, $\mathrm{EGF}_{\mathrm{corr}}$, and $\bar{r}$ are the data spectra, traveltime spectra, station spectra, EGF correction, and mean residual spectra, respectively. Note that $\bar{r}$ represents an average residual across all stations recording the event and is usually quite small, but may be nonzero because of the robust L1-norm weighting scheme in the inversion algorithm. The apparent spectra defined by equation (7) have the useful property that their mean value is equal to the inferred EGF-corrected source spectra: $\frac{1}{N}\sum_{j=1}^{N} \tilde{s}_{ij} = s_i$. This fact allows us to use a bootstrap resampling approach to assess the uncertainties with each corner frequency estimate as follows.

For each event, we first obtain a corner frequency estimate $\hat{f}_c$ using the EGF-corrected source spectra $s_i(f)$ as described in section 2.4. We next synthesize a set of $B = 100$ bootstrap-resampled source spectra by resampling with replacement from the N apparent spectra associated with the event and taking the mean. We then estimate the corner frequency of each of the B resampled source spectra to obtain a bootstrap distribution of $\hat{f}_c$ estimates for each event and use the bias-corrected, accelerated percentile technique [*Efron and Tibshirani*, 1994; *Carpenter and Bithell*, 2000] to derive confidence intervals for $\hat{f}_c$ at the 50% (i.e., the interquartile range) and 90% levels from the raw bootstrap distribution.

We use a similar approach to obtain uncertainties in M_0 by examining the variability in spectral moment $\tilde{\Omega}_{0(ij)}$ across all stations recording an event. In this case, the bootstrapping procedure is unnecessary, as the Ω_0 estimate is a linear function of the apparent spectra (a mean over the 2.4–4 Hz frequency band). We use the median absolute deviation in the apparent spectral moments of each event (i.e., the $\tilde{\Omega}_{0(ij)}$ of each event i) to quantify uncertainties in moment, which are typically of order 0.1 (in $\log_{10}$ units). Error estimates for $\hat{f}_c$ and $\hat{M}_0$ can then be used to derive confidence intervals for $\Delta\hat{\sigma}$ through propagation of errors (using equation (5)), though we caution that these measures of uncertainty are likely lower bounds, as they do not account for uncertainty in rupture velocity, and also do not address any of the epistemic or modeling uncertainties associated with the assumed source model.

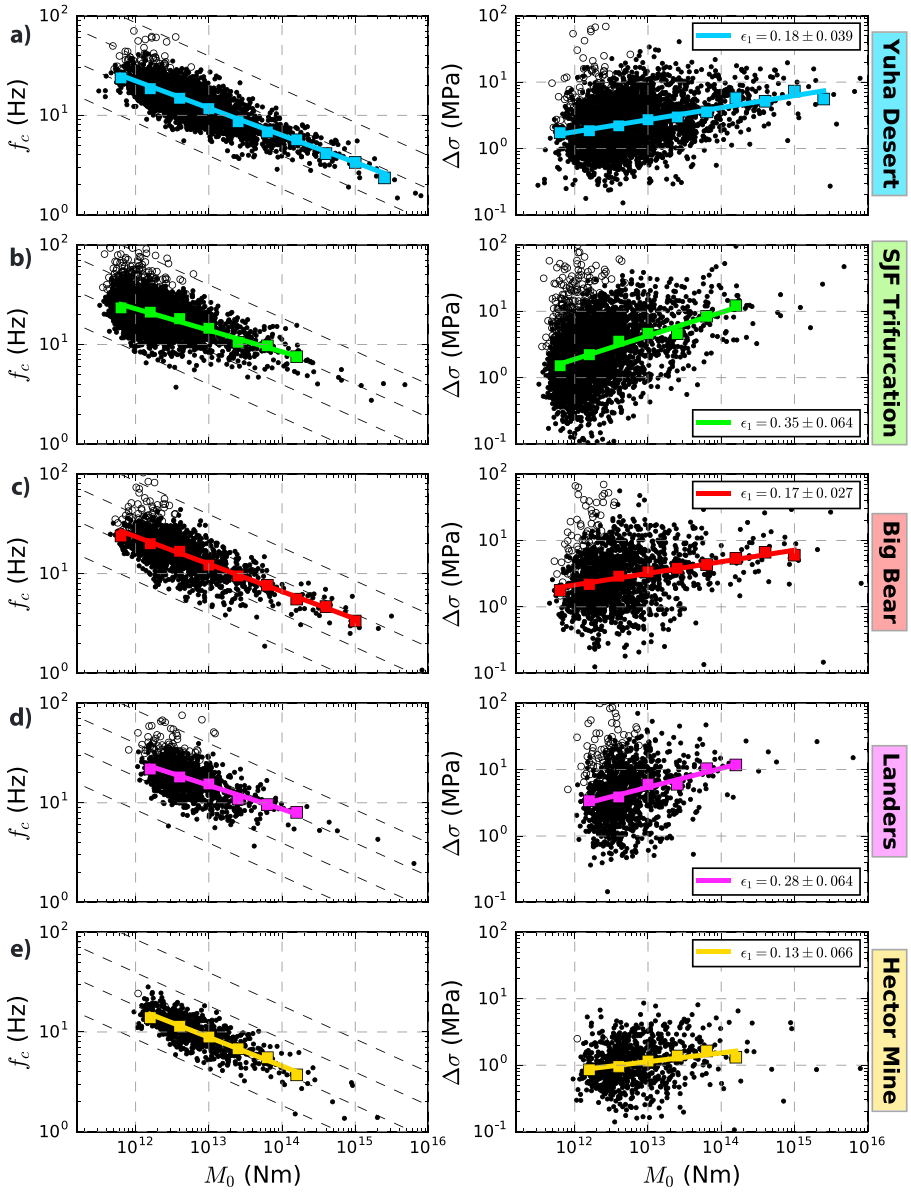

Figure 4. Scaling of (left column) corner frequency (f_c) and (right column) stress drop ($\Delta\sigma$) with seismic moment M_0. Each panel corresponds to one of the five study regions: (a) Yuha Desert, (b) San Jacinto Fault Trifurcation Zone, (c) Big Bear, (d) Landers, and (e) Hector Mine. In each panel, the black dots correspond to measurements of source properties for individual events, and the median f_c and $\Delta\sigma$ in M_0 bins of 0.4 ($\log_{10}$ Nm units) are marked with square symbols. The best fitting scaling parameter ϵ_1 and two sigma uncertainty for the binned data (obtained from weighted regression analysis; see text for details) is denoted in each right inset and plotted with a solid line. Events with poorly resolved corner frequencies due to bandwidth limitations are marked with open circles.

3. Results

We apply the spectral decomposition technique (section 2) to each of the five regions shown in Figure 1, performing a separate inversion for each region. Below, we present the salient features of the source parameter estimates for each region individually and compare the similarities and differences in the results across all regions. We focus in particular on the question of self-similarity (the scaling of $\Delta\sigma$ with M_0) and the observed spatiotemporal variations in stress drop on both regional and local scales.

3.1. Yuha Desert

The 2010 M_w 7.2 El Mayor-Cucapah earthquake is the largest event within the footprint of the SCSN during our study period (January 2002 through September 2016). The complex, bilateral faulting of the

El Mayor-Cucapah earthquake [*Wei et al.*, 2011; *Fletcher et al.*, 2014] triggered a dense cloud of aftershocks north of the USA-Mexico border in the Yuha Desert [*Kroll et al.*, 2013; *Hauksson et al.*, 2011]. Our Yuha Desert study region is composed primarily of these more northerly aftershocks, as the SCSN does not have an adequate azimuthal distribution of station coverage to make reliable spectral estimates for earthquakes to the south of the USA-Mexico border (Figure 1). The detailed relocation analysis of the first 2 months of aftershocks performed by *Kroll et al.* [2013] imaged the structural complexity of this region before the June 2010 M_w 5.7 Ocotillo earthquake, which triggered a second wave of seismicity in middle-to-late 2010 [*Hauksson et al.*, 2011].

In applying the improved spectral decomposition technique (section 2) to the Yuha Desert region, we obtain source parameter estimates for 3706 events that meet our minimum quality control criteria. Normalized uncertainties in corner frequency ($\Delta f_c/f_c$) tend to be higher for the lowest and highest magnitude events, which have corner frequencies at the limits of the signal bandwidth, but overall, the source spectra are well resolved. Corner frequency and stress drop show a moderate but consistent deviation from self-similarity, with median stress drop tending to increase as a function of seismic moment (Figure 4a). To quantify this more precisely, we define bins of width 0.4 in $\log_{10} M_0$ and compute the median stress drop for events in each bin. We then perform a weighted least squares regression analysis on the binned data to determine the best fitting scaling parameter ϵ_1 in a linear relation of the form

$$\log_{10} \Delta\sigma = \epsilon_0 + \epsilon_1 \log_{10} M_0. \tag{8}$$

Here the weights account for both the number of events in each bin and the median uncertainty in stress drop, where the latter depends primarily upon the uncertainty in corner frequency and secondarily on the uncertainty in moment (equation (5)). The scaling parameter $\epsilon_1 = 0.18$ ($\pm$ 0.039) inferred in this manner for the Yuha Desert is statistically positive, which is true for all five regions considered in this study (Figure 4). Median stress drop for this region is comparable to other regions (2.29 MPa), but of lower variability (Figure 5a, left), with nearly all events having stress drops in the range 0.5 to 20 MPa. Seismicity rates in the Yuha Desert region during our study period are greatest in 2010, following the April 2010 M_w 7.2 El Mayor-Cucapah and June 2010 M_w 5.7 Ocotillo events, and the $\mathbf{M} \geq 3$ events of this time period tend to exhibit high stress drops (Figure 5a, right). However, we do not observe any systematic time evolution in the stress drop, as events of comparable magnitude occurring at different times exhibit comparable stress drop. In other words, the conditional probability distribution of stress drop, given seismic moment, is stationary with time, but 2010 has an unusually large number of $\mathbf{M} \geq 3$ events due to its high seismicity rate.

We do observe significant spatial variations in median stress drop, with a tendency for events within the eastern portion of the Yuha Desert study region to have higher median stress drop than those in the west (Figure 6a). To check whether this observation is truly due to differences in source properties, and not a result of spatial variation in attenuation, we implemented a spatial interpolation-based EGF technique analogous to the (nearest neighbor) spatial EGF correction used by *Shearer et al.* [2006], finding the inferred spatial patterns in source parameters largely unchanged by the laterally varying EGF. This is not surprising, given the relatively small length scales (tens of kilometers) over which the region is defined. We further observe an increase in median corner frequency as a function of depth, larger than can be explained by the assumed increase in midcrustal shear velocity (Figure 7a).

3.2. San Jacinto Fault: Trifurcation Zone

The San Jacinto Fault (SJF) is the most seismically actively fault system in California [*Sanders et al.*, 1986; *Kagan et al.*, 2006; *Wdowinski*, 2009], and, along with the southern portion of the San Andreas Fault located to its east, accommodates the dominant portion of the plate boundary motion in Southern California [*Rockwell et al.*, 1990; *Fialko*, 2006; *Lindsey et al.*, 2014]. While the Anza section of the central SJF is notable for its lack of microseismicity and major earthquake sequences during historical times [*Sanders and Kanamori*, 1984; *Zöller and Ben-Zion*, 2014; *Rockwell et al.*, 2015; *Jiang and Fialko*, 2016], the intersection of the Coyote Creek, Clark, and Buck Ridge faults to the southeast of the Anza gap is responsible for approximately 10% of all earthquake production in Southern California during our study period (2002–2016). This region of particularly dense seismicity has produced multiple distinct sequences of $\mathbf{M} \geq 4$ earthquakes distributed across the three subparallel faults that comprise the trifurcation zone [*Allam et al.*, 2014; *Ross et al.*, 2017], including the recent (June 2016) M_w 5.2 Borrego Springs event. Though the main shocks within these sequences show predominantly strike-slip mechanisms, the individual faulting structures within the trifurcation zone are particularly complex,

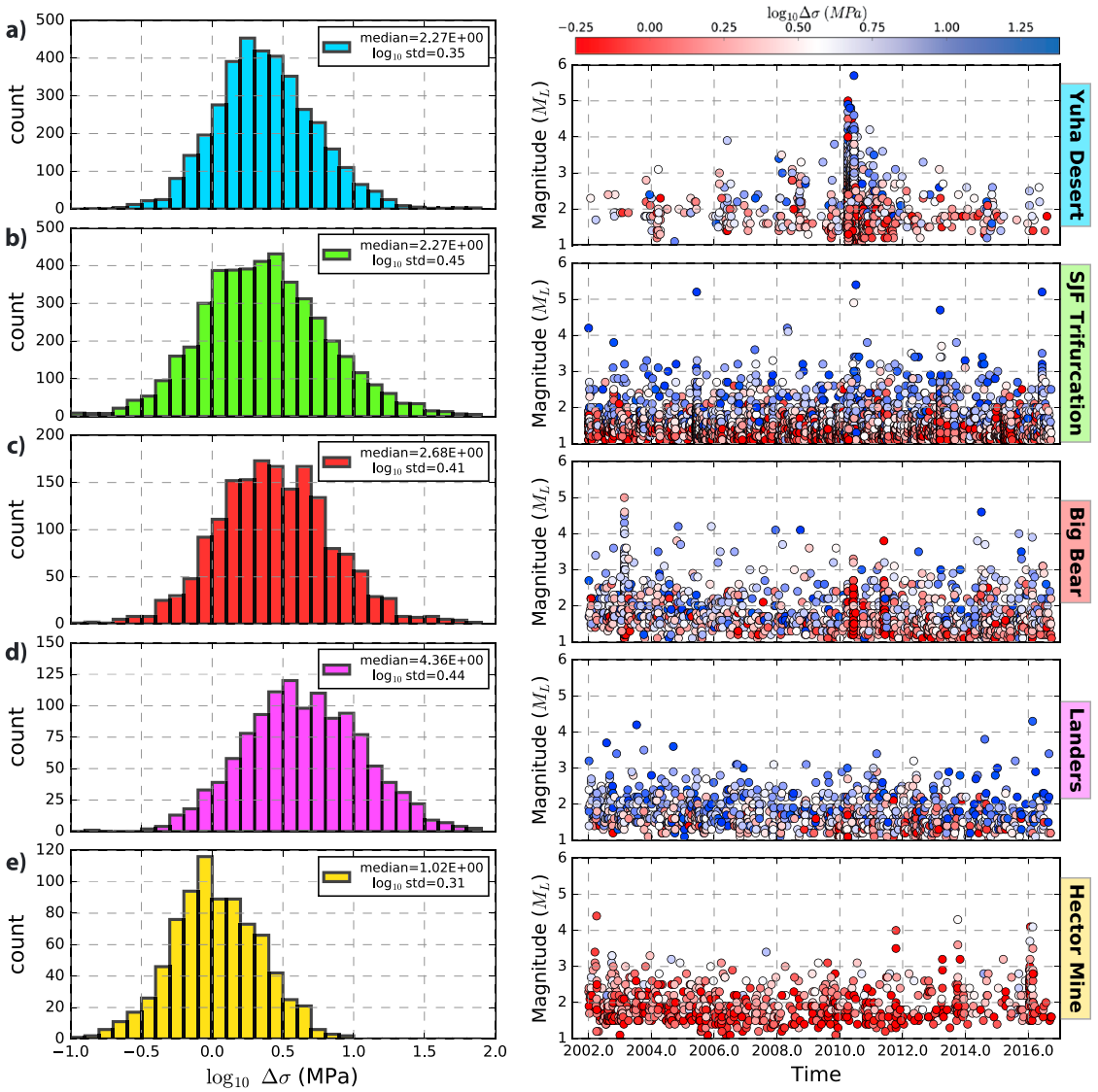

Figure 5. Histograms of stress drop (left column) and magnitude-time plots (right column) for each of the five study regions: (a) Yuha Desert, (b) San Jacinto Fault Trifurcation Zone, (c) Big Bear, (d) Landers, and (e) Hector Mine. Median and standard deviation values ($\log_{10}$ MPa) of the stress drop distributions are marked in the histogram insets (Figure 5, left column). Events are color coded by stress drop in each magnitude-time plot (Figure 5, right column), with bluer colors indicating higher stress drop (more high-frequency energy).

with high-resolution tomography [*Allam et al.*, 2014; *Lin et al.*, 2016] and studies of fault zone-trapped waves [*Li and Vernon*, 2001; *Lewis et al.*, 2005; *Ross and Ben-Zion*, 2015] indicating the prevalence of damage zones.

We use the spectral decomposition technique (section 2) to obtain source parameter estimates for 4564 earthquakes in the SJF trifurcation zone region. The median stress drop (2.27 MPa) is comparable to that of the Yuha region. However, the inferred stress drops for events within the SJF trifurcation zone exhibit greater heterogeneity, as evidenced by the significantly larger standard deviation in the stress drop distribution than is observed for Yuha (Figure 5b, left). This heterogeneity may reflect the tectonic complexity of this region, which is characterized by a hierarchical network of structures that accommodate a diverse set of faulting mechanisms and varying levels of recent seismic activity [*Sanders and Kanamori*, 1984; *Li and Vernon*, 2001; *Lewis et al.*, 2005].

Seismicity within the SJF trifurcation zone is also notable for its strong deviation from classical self-similarity, with median stress drop increasing by nearly a factor of 10 across the magnitude range considered in our data set (Figure 4b). The scaling parameter $\epsilon_1 = 0.35$ ($\pm$ 0.064) inferred using the weighted regression procedure

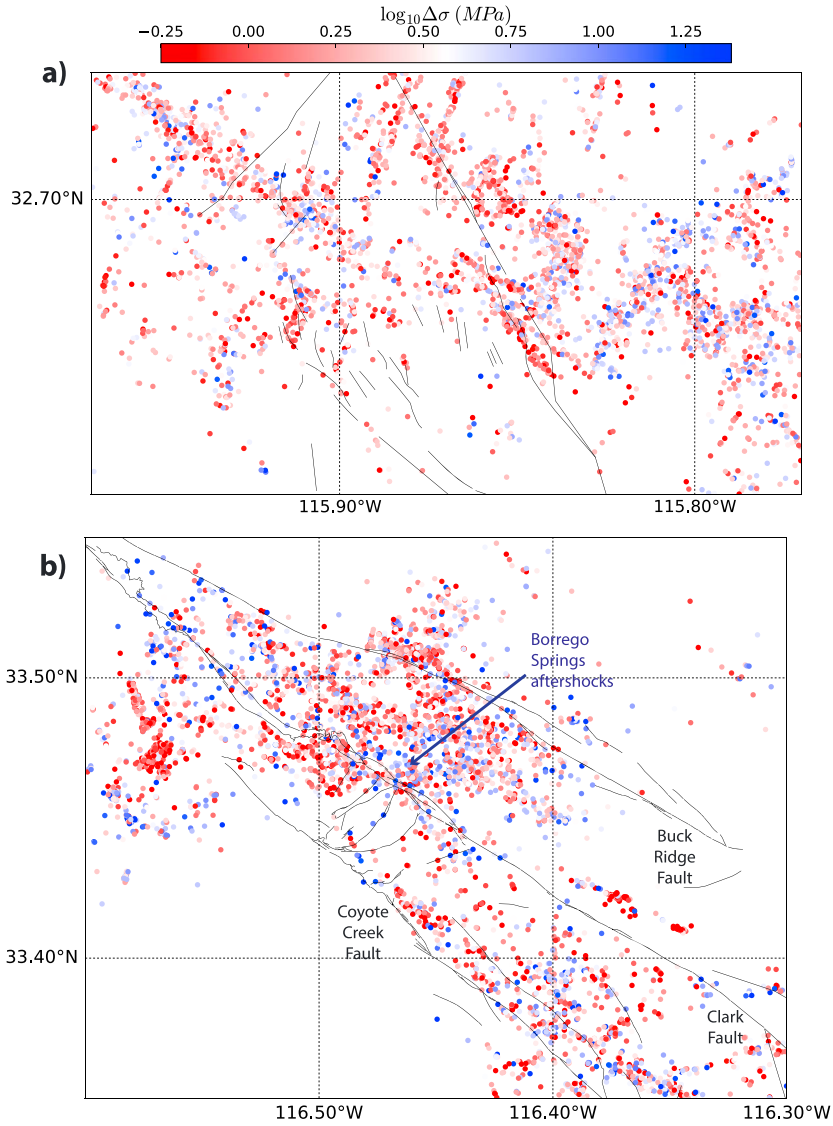

Figure 6. Map view of source parameter estimates for (a) Yuha Desert and (b) San Jacinto Fault Trifurcation Zone regions. Events are color coded by stress drop in each map, with bluer colors indicating higher stress drop (more high-frequency energy).

described in section 3.1 is the highest of any of the five regions in our study and would be on the higher end of previously reported values, which typically are in the range of 0.1–0.4 [*Mayeda and Walter*, 1996; *Izutani and Kanamori*, 2001; *Kanamori and Rivera*, 2004; *Takahashi et al.*, 2005; *Mayeda et al.*, 2005; *Venkataraman et al.*, 2006; *Pacor et al.*, 2016a]. This trend in scaling is persistent over the duration of our study period (Figure 5b, right) and may in part be related to fact that the larger (**M** ≥ 3.5) events in the trifurcation zone tend to occur along the three major fault strands, while microseismicity preferentially occurs in the off-fault and intrafault regions [*Ross et al.*, 2017]. A full exploration into the causative mechanisms of this strong regional trend in scaling is, however, beyond the scope of this study.

Despite the lack of clear time dependence in scaling, there does appear to be some variability in the distribution of stress drops within individual earthquake sequences. Of particular interest is the June 2016 M_w 5.2 Borrego Springs event, which is the most recent prominent main shock in our data set. Both the Borrego Spring event and its aftershocks exhibit unusually high stress drop values compared to other events with equivalent moment (Figure 5b, right). The Borrego Springs event occurred on the Clark Fault, near the site of two $M_w \geq 4$ events that occurred in 2008 but were of much lower stress drop. Most of the Borrego Springs

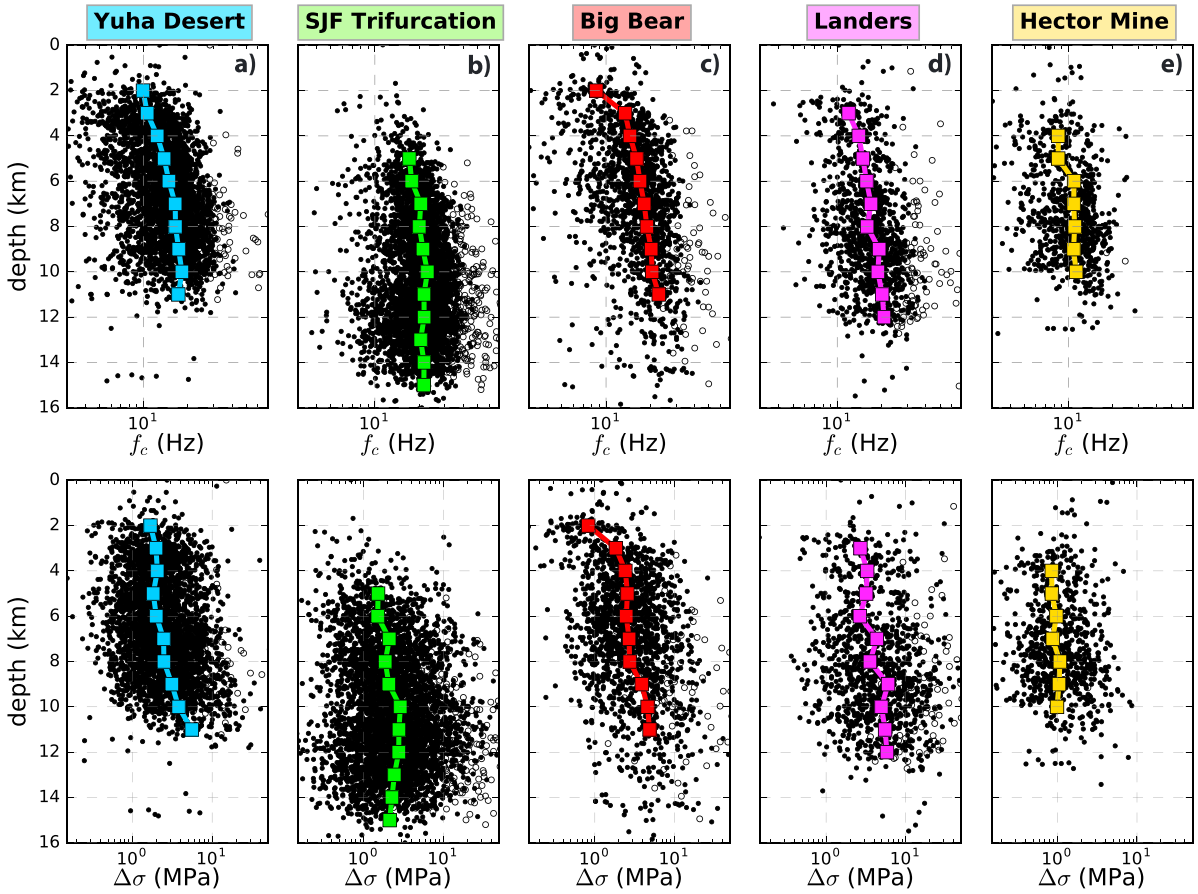

Figure 7. Depth dependence of (top row) corner frequency (f_c) and (bottom row) stress drop ($\Delta\sigma$) for each of the five study regions: (a) Yuha Desert, (b) San Jacinto Fault Trifurcation Zone, (c) Big Bear, (d) Landers, and (e) Hector Mine. In each plot, the black dots correspond to measurements of source properties for individual events, and the median f_c and $\Delta\sigma$ in depth bins of 1 km are marked with solid lines. Events with poorly resolved corner frequencies due to bandwidth limitations are marked with open circles.

aftershocks occurred between the Clark and Buck Ridge faults, at depths of ~12 km and on previously inactive structures that are almost orthogonal to the primary strands. These events are visually prominent in the map view shown in Figure 6b due to their high median stress drop.

3.3. Mojave Desert Regions: Big Bear, Landers and Hector Mine

In contrast to the Yuha Desert and San Jacinto Fault regions examined above, seismicity within the Big Bear, Landers, and Hector Mine regions of the Mojave Desert occurs to the east of the main Pacific-North American plate boundary. These regions comprise the southern portion of the Eastern California Shear Zone (ECSZ), a diffuse deformational belt characterized by a complex distribution of incipient faulting structures [*VanWormer and Ryall*, 1980; *Faulds and Henry*, 2008; *Wesnousky et al.*, 2012]. Studies of earthquake hazard in the ECSZ became more exigent with the occurrence of the 1992 Landers (M_w 7.3), 1992 Big Bear (M_w 6.5), and 1999 Hector Mine (M_w 7.1) earthquakes, three of the largest events in Southern California in the past century [*Hauksson et al.*, 1993; *Cohee and Beroza*, 1994; *Wald and Heaton*, 1994; *Fialko*, 2004]. Stress changes from these events had a significant influence on the local stress field and seismicity during their immediate aftermath [e.g., *Hauksson*, 1994; *King et al.*, 1994; *Hardebeck et al.*, 1998; *Lin and Stein*, 2004]. Our study period begins in 2002 and thus considers only the longer-term aftershocks of these events and present-day background seismicity within each region. In our study, we perform the spectral decomposition for each region independently in order to mitigate the effects of differences in local attenuation on source spectral estimates but present the results for all three regions here, as they form a coherent tectonic zone within the southern ECSZ.

We obtain source parameter estimates for 1723, 1215, and 810 events in the Big Bear, Landers, and Hector Mine regions, respectively. Despite their proximity, we observe quantifiable differences in the source properties of earthquakes in each region. Earthquakes in the Landers rupture zone are characterized by significantly higher

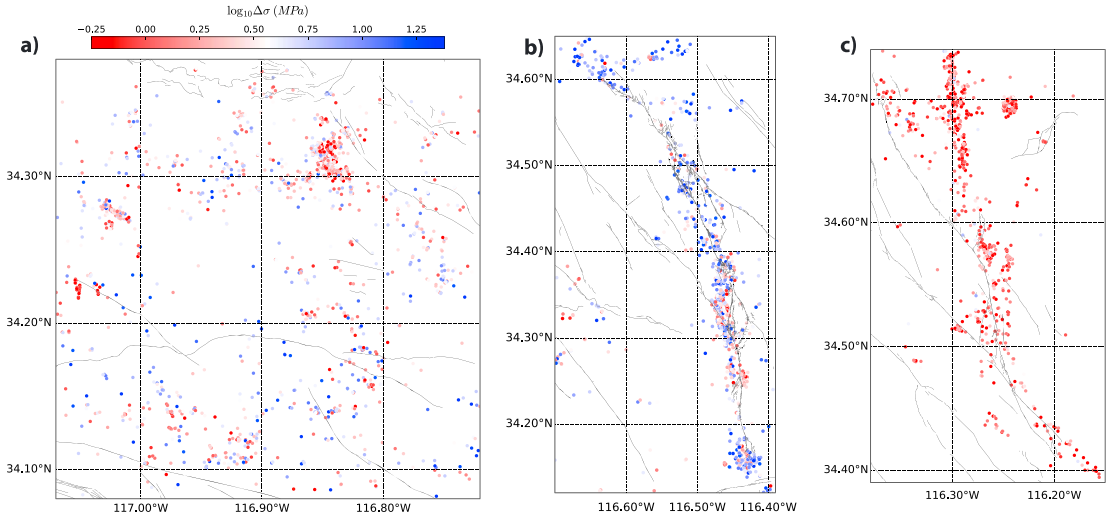

Figure 8. Map view of source parameter estimates for the (a) Big Bear, (b) Landers, and (c) Hector Mine regions. Events are color coded by stress drop in each map, with bluer colors indicating higher stress drop (more high-frequency energy).

median stress drop (4.36 MPa) than those in the Hector Mine rupture zone (1.02 MPa), with Big Bear (2.68 MPa) falling in between (Figures 5c–5e). The distribution of stress drop is also more variable in the Landers and Big Bear regions than in Hector Mine. Applying the binning procedure and the weighted regression analysis described in section 3.1, we also observe a moderate increase in median stress drop with moment in each of the Big Bear ($\epsilon_1 = 0.17 \pm 0.027$), Landers ($\epsilon_1 = 0.28 \pm 0.064$), and Hector Mine ($\epsilon_1 = 0.13 \pm 0.066$) regions. We note, however, that the inferred scaling parameters (ϵ_1) are more poorly constrained for these three regions due to the relative scarcity of $\mathbf{M} \geq 3$ events, as compared to the dense seismicity of the Yuha or SJF regions.

Although localized clusters of higher and lower median stress drops can be discerned in each of the three regions (Figure 8), the spatial variations are most apparent within the Landers rupture zone. Specifically, we observe significant along-strike variations in median stress drop, with higher values in the northernmost and southernmost segments, and lower values in the central portion of the Landers rupture (Figure 8b), a pattern similar to that found in the stress drop study of *Shearer et al.* [2006] for Landers aftershocks from 1992 through 2001. Overall, there appears to be a rough anticorrelation between the stress drops of Landers aftershocks (both early and late) and the magnitude of fault slip during the 1992 rupture, during which peak values of fault slip were observed along the central portion of the rupture and lower slip at the northern and southern tips and auxiliary fault segments [*Fialko*, 2004]. The lack of significant pre–main shock seismicity in this region makes it hard to assess whether this stress drop pattern is a long-standing feature (perhaps caused by local variations in fault strength, with the stronger zones both inhibiting slip during the Landers rupture and producing ambient seismicity with higher stress drops), or whether it reflects stress changes caused by the main shock rupture, with lowered stress in the high-slip regions and increased stress near the fault tips. Unfortunately, the large uncertainties in finite slip models for the Landers main shock (as evidenced by the substantial differences among the published models [e.g., *Mai and Thingbaijam*, 2014]) complicate more detailed comparisons between aftershock stress drops and main shock slip at finer spatial scales.

Some evidence for long-lived spatial variations of small earthquake stress drops was provided by a stress drop study at Parkfield [*Allmann and Shearer*, 2007], in which the overall pattern of high and low stress drop regions was unaffected by the 2004 **M**6.0 Parkfield earthquake. Although the Parkfield section of the San Andreas Fault is distinctly different from our study regions (having a single well-defined fault, and many areas of fault creep), it is nonetheless interesting that the spatial patterns we observe in stress drop appear to persist over long time periods. For example, the spatial heterogeneity in source parameters observed within the Mojave Desert regions remains largely unchanged from the study of *Shearer et al.* [2006], who considered a completely independent source parameter data set ending in year 2001. The long-term persistence of these trends—lower stress drop in the Hector Mine rupture zone, higher stress drop in the Landers rupture zone, with significant along-strike variations—supports the notion that there exist real spatial variations in median

stress drop that are both quantifiable and somewhat predictable due to their stationarity in time. If so, this has important implications for hazard assessments that use seismically determined stress drop or a related proxy stress parameter as input for ground motion prediction equations [*Yenier and Atkinson*, 2014; *Atkinson et al.*, 2015]. Also of interest from a hazard perspective is that the shallowest seismicity (observed primarily in the Big Bear region) is characterized by particularly low stress drops (Figure 7c). At more intermediate depths, corner frequency increases with depth at roughly the same rate as the shear wave speed (and hence, mean rupture velocity), such that the inferred stress drop estimates remain approximately depth-invariant.

4. Discussion

The observed trends in earthquake source properties within the five regions have important implications for our understanding of earthquake rupture and seismic hazard. As such, it is worth examining in closer detail the limitations of the methods applied to obtain these source parameter estimates, and their potential influence on the results presented here. These limitations fall into two main classes: (1) limitations in the ability of the spectral decomposition method to isolate the source spectrum from the raw waveform data and (2) limitations in the source spectral model to adequately characterize the salient properties of earthquake rupture.

Addressing (1) first, a key advantage of the spectral decomposition method is that it provides an empirical and completely nonparametric framework for partitioning the observed spectra into source, path, and station terms, with no need to explicitly evaluate the instrument response or model attenuation along the raypath. This framework, while designed to minimize the tradeoffs between source and path effects, may still fail to adequately resolve the source term, especially in circumstances where the ratio of the number of input, observed spectra, to desired, output source spectra is small. The EGF correction that is inferred from the shape of stacked source spectra (section 2.3) is an essential step in the spectral decomposition algorithm, as it removes nonsource effects that are common to all travel paths. This includes both near-source and near-receiver attenuation, which, if left uncorrected, can introduce an artificial f_{max} into the spectra that may bias source parameter estimates [*Hanks*, 1982; *Anderson and Hough*, 1984; *Anderson*, 1986]. We do not believe that uncorrected high-frequency attenuation is causing problems in our analysis for several reasons: (1) we explicitly require that all of the individual spectra we analyze have signal-to-noise of five or greater out to the 25 Hz upper bandwidth and (2) we see no evidence for any sharp change in our traveltime terms or in our EGFs as frequency approaches 25 Hz. Certainly, attenuation will limit the ability to resolve corner frequencies above 25 Hz, but accurately determining these corner frequencies is not crucial for our analysis.

However, the spectral stacking procedure requires a reasonable distribution of events at different magnitudes over a relatively small length scale (tens of kilometers). This does not present a significant obstacle for the five regions considered here, which have relatively dense seismicity sampling a wide range of magnitudes (**M** 1 to 5) and are well recorded by modern broadband and short-period SCSN stations. It is important, however, to keep these considerations in mind in future applications of the spectral decomposition technique to scenarios with sparse seismicity or station coverage.

The second limitation—the possible inadequacy of the commonly applied Brune-type, omega-squared (ω^{-2}) source model to describe the earthquake rupture process—presents a more serious problem for the events considered here. The observed deviation from self-similarity, in which stress drop appears to increase as a function of seismic moment ($\epsilon_1 > 0$), is based on the assumption that the high-frequency spectral falloff rate (n in equation (4)) is 2, as in the classical ω^{-2} model [*Aki*, 1967]. There is, however, a fundamental tradeoff between ϵ_1 and n, as shown schematically in Figure 9 for the Yuha Desert region (the other four regions considered in this study exhibit a similar effect). If we instead allow for $n < 2$ (gentler spectral falloff), the data once again become consistent with self-similarity; the difference in misfit between the $\epsilon_1 > 0, n = 2$ and $\epsilon_1 = 0, n < 2$ models is only 1.2%. This makes intuitive sense if we consider that our fundamental observation is that the source spectra of larger events contain more high-frequency content than would be predicted by a self-similar Brune model. The tradeoff between ϵ_1 and n occurs because the high-frequency falloff rate substantially affects the results only well above the corner frequency, a portion of the spectra that is observable only for the larger events in our data set. There are two different end-member ways of explaining the high frequencies we observe for the larger events: we can fix the spectral falloff and relax the assumption of self-similarity (Figure 9a) or we can assume that earthquakes are (on average) self-similar and allow for gentler spectral falloff (Figure 9b).

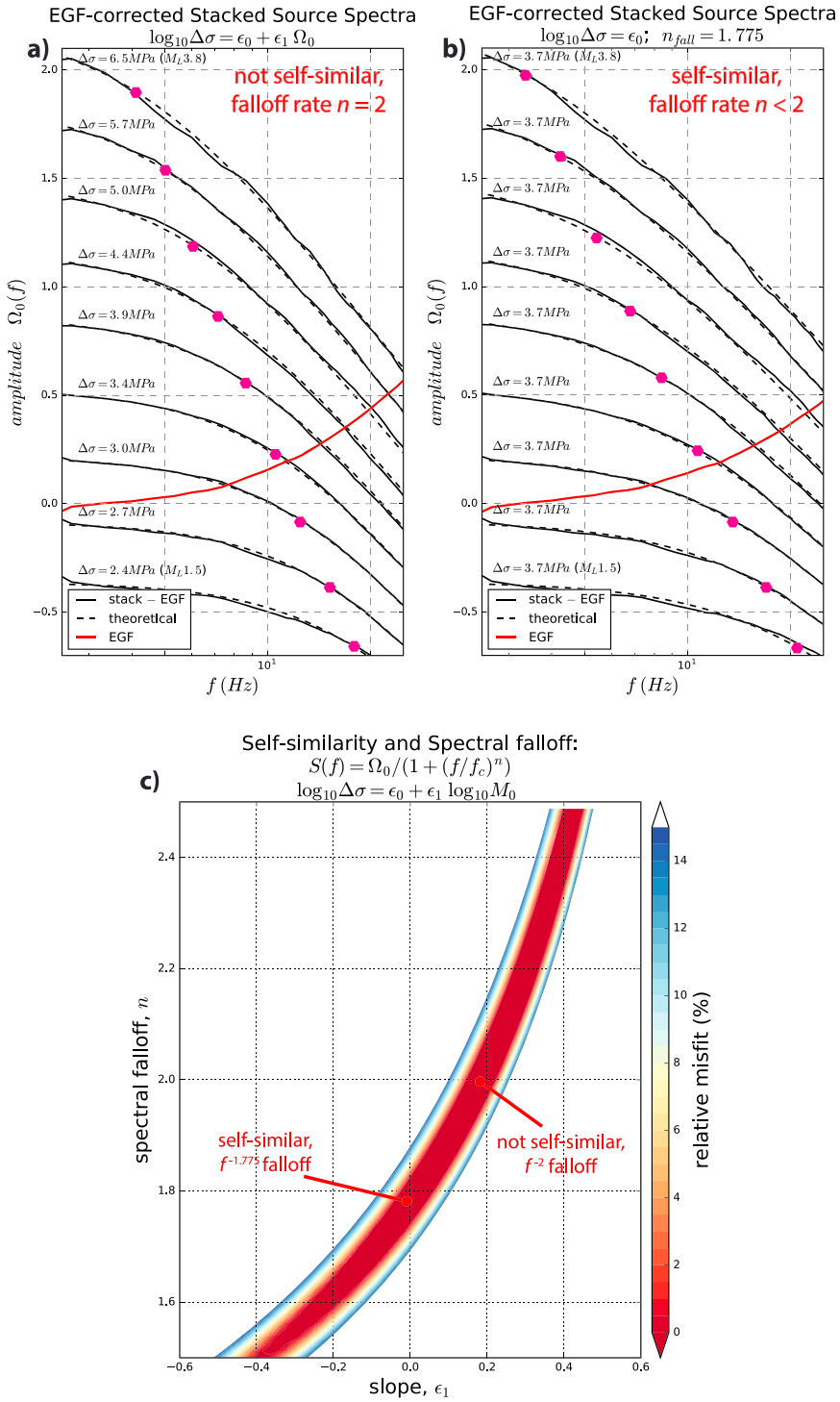

Figure 9. Example showing the tradeoff between stress drop scaling parameter ϵ_1 and spectral falloff rate n, for stacked source spectra from the Yuha Desert region (results are similar for the other regions considered in this study). (a) EGF-corrected, stacked source spectra (solid black lines, binned by spectral moment Ω_0) assuming a source model with ω^{-2} spectral falloff rate ($n = 2$) and scaling parameter $\epsilon_1 > 0$. In this model, $\log_{10}\Delta\sigma$ is permitted to vary linearly with $\log_{10} M_0$. (b) EGF-corrected source spectra (solid black lines, binned by spectral moment Ω_0), now assuming a source model with lower spectral falloff rate ($n < 2$) and fixed scaling parameter $\epsilon_1 = 0$. In this model, $\Delta\sigma$ is constrained to be invariant with M_0. (c) Contour plot of the relative misfit between the observed (EGF-corrected) and theoretical stacked spectra, plotted as a function of scaling parameter (ϵ_1, x axis) and high-frequency falloff rate (n, y axis). Source models that assume $n = 2$ (an ω^{-2} model) require $\epsilon_1 > 0$, while source models that assume $\epsilon_1 = 0$ (a self-similar model) require $n < 2$.

We focus on the former approach for the purposes of this study because it makes our source parameter estimates (corner frequency f_c and stress drop $\Delta\sigma$) more directly comparable to those of other studies, which are typically derived under the assumption of an ω^{-2} model. The discussion above, however, demonstrates that the absolute values of these source parameter estimates depend strongly on modeling assumptions. This makes it difficult to interpret f_c and $\Delta\sigma$ directly in terms of actual physical properties of the earthquake source, such as the source dimension or average static stress drop. Moreover, the tradeoff complicates studies of earthquake source scaling, as the inferred scaling parameter will in turn depend on the assumed falloff rate (again, typically fixed to 2 in such studies). Though the high-frequency falloff n must be greater than 1.5 to bound the radiated energy [*Walter and Brune*, 1993], this limitation only applies in the high-frequency limit, i.e., not to intermediate falloff rates that may occur in double-corner frequency models. For single-corner frequency models, if the true falloff rate falls anywhere in the range $1.5 < n < 2$, the scaling will be less intense than that inferred with $n = 2$, as is typically assumed for such studies [*Kanamori and Rivera*, 2004]. Finally, we note that the observed scaling relationships are pertinent only to the magnitude range that comprises the bulk of our data set ($1 \leq \mathbf{M} \leq 4$) and should not be extrapolated without further study. Independent of these issues, we can still pose the following questions: what are the underlying causes of the observed deviations from classical source models, and what are the broader implications for our understanding of earthquake rupture processes?

Brune [1970] developed an instantaneous rupture model for a circular crack that related the source radius of an earthquake to the inverse of the corner frequency of the calculated source spectra. This model was later extended by *Madariaga* [1976] and others who considered more realistic circular crack models in which the rupture propagates at a constant fraction of the shear wave velocity. However, real source spectra, especially those of pulse-like ruptures, can be much more complex and may be characterized by several timescales (and hence corner frequencies), notably those related to the total rupture duration and to the duration of slip at a given point on the fault [e.g., *Haskell*, 1969; *Luco*, 1985; *Lin et al.*, 2016]. Resolution of these features in real source spectra is challenging due to the inherent noise and bandwidth limitations of the data, but a number of studies of larger earthquakes [e.g., *Papageorgiou and Aki*, 1983; *Joyner*, 1984; *Atkinson*, 1990; *Denolle and Shearer*, 2016] have provided evidence for source spectra with multiple corners and intermediate spectral falloffs ($n < 2$), the details of which can likewise be scale dependent [*Walter et al.*, 2006].

We do not attempt to resolve multiple corners within the source spectra in our study, as lower magnitude events have poor signal-to-noise within the higher-frequency bands in which the secondary corner would be expected to occur. However, the presence of multiple corners, even if they cannot be independently resolved in the spectra, could account for the observed tradeoff between high-frequency falloff rate n and self-similarity ϵ_1. Further complexity in the rupture process, including directivity effects [e.g., *Boatwright*, 1980; *Pacor et al.*, 2016b; *Ross et al.*, 2016], fault-roughness [e.g., *Madariaga et al.*, 2006; *Dunham et al.*, 2011; *Trugman and Dunham*, 2014], and scale-dependent frictional properties or dynamic weakening mechanisms [*Brodsky and Kanamori*, 2001; *Abercrombie and Rice*, 2005; *Cocco et al.*, 2016] may also produce the same effect. Though it is difficult to discriminate among these plausible causal mechanisms, their unifying feature—source complexity beyond that of a circular crack—makes it worth exploring alternative or nonparametric means for directly comparing source spectra, rather than comparing source parameter derivative of an assumed model [e.g., *Uchide and Imanishi*, 2016].

The results presented here also bear significance for seismic hazard assessment. Ground motion prediction equations (GMPEs) are fundamental to hazard assessments, and source spectral studies that characterize regional variations in stress drop provide valuable constraints for the source terms of modern GMPEs, which are becoming increasingly regionalized [*Bozorgnia et al.*, 2014; *Yenier and Atkinson*, 2015; *Douglas and Edwards*, 2016]. Previous work [e.g., *Allmann and Shearer*, 2009; *Oth*, 2013; *Uchide et al.*, 2014] has provided compelling evidence for regional variations in median stress drop. Here we find in addition that both median stress drop and the intensity of the apparent deviation from self-similarity may vary regionally, with the San Jacinto Fault trifurcation zone being of particular note in this regard (Figure 4). Accurately characterizing such variations may help reconcile the well-known difference in scatter between the $\Delta\sigma$ of GMPEs (stress parameter) and the $\Delta\sigma$ of source spectral estimates (stress drop) [*Atkinson and Beresnev*, 1997; *Cotton et al.*, 2013; *Atkinson et al.*, 2015], although it is worth again cautioning that the scaling relationships inferred here likely do not extrapolate to the higher-magnitude ($\mathbf{M} > 4$) events that cause the most damaging ground motions. Future studies should examine the robustness of these preliminary observations over wider magnitude ranges and larger

spatial scales and explore how the modeling limitations of source parameter estimates may influence the relationship between seismically inferred stress drop and observed ground motion.

5. Conclusions

We describe an improved spectral decomposition approach to compute earthquake source parameters that is suitable for analyzing large data sets containing thousands or more events. The technique uses an iterative, robust least squares algorithm to partition the observed waveform spectra into source, site, and traveltime-dependent path terms. Unlike previous methods of its kind, this technique requires no assumption about self-similarity in earthquake source parameters. We leverage this improvement to explore variations in source parameters and source scaling within five regions of active, contemporary (2002–2016) seismicity in Southern California. In each region, we find that if one assumes the classical, ω^{-2} high-frequency falloff rate, the data are most consistent with an increase of stress drop with moment, in direct contrast to the self-similar paradigm. We show, however, that this conclusion is model dependent, with the inferred deviation from self-similarity trading off with the assumed high-frequency falloff rate. Independent of these parametric limitations, the source spectra of the larger magnitude earthquakes in this study contain greater high-frequency content than would be predicted by a self-similar model with ω^{-2} falloff. This observation, along with the evidence we present for regional, local, and depth-dependent variations in earthquake source parameters, may provide important constraints for seismic hazard assessments and for our understanding of earthquake rupture processes.

Acknowledgments
The waveform data used in this study are archived by and are publicly available from the Southern California Earthquake Data Center (http://scedc.caltech.edu/, last accessed 4 December 2016). The source parameter catalogs associated with this study are available in the supporting information of this manuscript (supporting information Data Sets S1 through S5). This manuscript is based upon work supported by the National Science Foundation Graduate Research Fellowship Program (NSFGRFP) under grant DGE-1144086. Additional support was provided by the Southern California Earthquake Center (SCEC) under grant 16020. We wish to thank Annemarie Baltay and Bill Walter for their thoughtful and constructive reviews, as well as Rachel Abercrombie, Zachary Ross, Egill Hauksson, Yuri Fialko, and Adrian Borsa for lively intellectual discussions that contributed to the content of this manuscript.

References

Abercrombie, R. E. (2013), Comparison of direct and coda wave stress drop measurements for the Wells, Nevada, earthquake sequence, *J. Geophys. Res. Solid Earth*, *118*, 1458–1470, doi:10.1029/2012JB009638.

Abercrombie, R. E. (2015), Investigating uncertainties in empirical Green's function analysis of earthquake source parameters, *J. Geophys. Res. Solid Earth*, *120*, 4263–4277, doi:10.1002/2015JB011984.

Abercrombie, R. E., and J. R. Rice (2005), Can observations of earthquake scaling constrain slip weakening?, *Geophys. J. Int.*, *162*(2), 406–424, doi:10.1111/j.1365-246X.2005.02579.x.

Abercrombie, R. E., S. Bannister, J. Ristau, and D. Doser (2017), Variability of earthquake stress drop in a subduction setting, the Hikurangi Margin, New Zealand, *Geophys. J. Int.*, *208*, 306–320, doi:10.1093/gji/ggw393.

Akaike, H. (1974), A new look at the statistical model identification, *IEEE Trans. Automatic Control*, *19*(6), 716–723, doi:10.1109/TAC.1974.1100705.

Aki, K. (1967), Scaling law of seismic spectrum, *J. Geophys. Res.*, *72*(4), 1217–1231, doi:10.1029/JZ072i004p01217.

Allam, A. A., Y. Ben-Zion, I. Kurzon, and F. Vernon (2014), Seismic velocity structure in the Hot Springs and Trifurcation areas of the San Jacinto fault zone, California, from double-difference tomography, *Geophys. J. Int.*, *198*(2), 978–999, doi:10.1093/gji/ggu176.

Allmann, B. P., and P. M. Shearer (2007), Spatial and temporal stress drop variations in small earthquakes near Parkfield, California, *J. Geophys. Res.*, *112*, B04305, doi:10.1029/2006JB004395.

Allmann, B. P., and P. M. Shearer (2009), Global variations of stress drop for moderate to large earthquakes, *J. Geophys. Res.*, *114*, B01310, doi:10.1029/2008JB005821.

Anderson, J. G. (1986), Implication of attenuation for studies of the earthquake source, in *Earthquake Source Mechanics*, edited by S. Das, J. Boatwright, and C. H. Scholz, pp. 311–318, AGU, Washington, D. C., doi:10.1029/GM037p0311.

Anderson, J. G., and S. E. Hough (1984), A model for the shape of the Fourier amplitude spectrum of acceleration at high frequencies, *Bull. Seismol. Soc. Am.*, *74*(5), 1969–1993.

Atkinson, G., K. Assatourians, B. Cheadle, and W. Greig (2015), Ground motions from three recent earthquakes in Western Alberta and Northeastern British Columbia and their implications for induced-seismicity hazard in eastern regions, *Seismol. Res. Lett.*, *86*(3), 1022–1031, doi:10.1785/0220140195.

Atkinson, G. M. (1990), A comparison of Eastern North American ground motion observations with theoretical predictions, *Seismol. Res. Lett.*, *61*(3–4), 171–180, doi:10.1785/gssrl.61.3-4.171.

Atkinson, G. M., and I. Beresnev (1997), Don't call it stress drop, *Seismol. Res. Lett.*, *68*(1), 3–4, doi:10.1785/gssrl.68.1.3.

Baltay, A., G. Prieto, and G. C. Beroza (2010), Radiated seismic energy from coda measurements and no scaling in apparent stress with seismic moment, *J. Geophys. Res.*, *115*, B08314, doi:10.1029/2009JB006736.

Baltay, A., S. Ide, G. Prieto, and G. Beroza (2011), Variability in earthquake stress drop and apparent stress, *Geophys. Res. Lett.*, *38*, L06303, doi:10.1029/2011GL046698.

Boatwright, J. (1980), A spectral theory for circular seismic sources; simple estimates of source dimension, dynamic stress drop, and radiated seismic energy, *Bull. Seismol. Soc. Am.*, *70*(1), 1–27.

Bozorgnia, Y., et al. (2014), NGA-West2 Research Project, *Earthquake Spectra*, *30*(3), 973–987, doi:10.1193/072113EQS209M.

Brodsky, E. E., and H. Kanamori (2001), Elastohydrodynamic lubrication of faults, *J. Geophys. Res.*, *106*(B8), 16,357–16,374, doi:10.1029/2001JB000430.

Brune, J. N. (1970), Tectonic stress and the spectra of seismic shear waves from earthquakes, *J. Geophys. Res.*, *75*(26), 4997–5009, doi:10.1029/JB075i026p04997.

Calderoni, G., A. Rovelli, and S. K. Singh (2013), Stress drop and source scaling of the 2009 April L'Aquila earthquakes, *Geophys. J. Int.*, *192*(1), 260–274, doi:10.1093/gji/ggs011.

Carpenter, J., and J. Bithell (2000), Bootstrap confidence intervals: When, which, what? A practical guide for medical statisticians, *Stat. Med.*, *19*(9), 1141–1164, doi:10.1002/(SICI)1097-0258(20000515)19:9<1141::AID-SIM479>3.0.CO;2-F.

Castro, R. R., J. G. Anderson, and S. K. Singh (1990), Site response, attenuation and source spectra of *S* waves along the Guerrero, Mexico, subduction zone, *Bull. Seismol. Soc. Am.*, *80*(6A), 1481–1503.

Choy, G. L., and J. L. Boatwright (1995), Global patterns of radiated seismic energy and apparent stress, *J. Geophys. Res.*, *100*(B9), 18,205–18,228, doi:10.1029/95JB01969.
Cocco, M., E. Tinti, and A. Cirella (2016), On the scale dependence of earthquake stress drop, *J. Seismol.*, *20*, 1151–1170, doi:10.1007/s10950-016-9594-4.
Cohee, B. P., and G. C. Beroza (1994), Slip distribution of the 1992 Landers earthquake and its implications for earthquake source mechanics, *Bull. Seismol. Soc. Am.*, *84*(3), 692–712.
Cotton, F., R. Archuleta, and M. Causse (2013), What is sigma of the stress drop?, *Seismol. Res. Lett.*, *84*(1), 42–48, doi:10.1785/0220120087.
Denolle, M. A., and P. M. Shearer (2016), New perspectives on self-similarity for shallow thrust earthquakes, *J. Geophys. Res. Solid Earth*, *121*, 6533–6565, doi:10.1002/2016JB013105.
Douglas, J., and B. Edwards (2016), Recent and future developments in earthquake ground motion estimation, *Earth Sci. Rev.*, *160*, 203–219, doi:10.1016/j.earscirev.2016.07.005.
Dunham, E. M., D. Belanger, L. Cong, and J. E. Kozdon (2011), Earthquake ruptures with strongly rate-weakening friction and off-fault plasticity: Part 2. Nonplanar faults, *Bull. Seismol. Soc. Am.*, *101*(5), 2308–2322, doi:10.1785/0120100076.
Efron, B., and R. J. Tibshirani (1994), *An Introduction to the Bootstrap*, CRC Press, Boca Raton, Fla.
Faulds, J. E., and C. D. Henry (2008), Tectonic influences on the spatial and temporal evolution of the Walker Lane: An incipient transform fault along the evolving Pacific-North American plate boundary, *Ariz. Geol. Soc. Digest*, *22*, 437–470.
Fialko, Y. (2004), Probing the mechanical properties of seismically active crust with space geodesy: Study of the coseismic deformation due to the 1992 M_w7.3 Landers (Southern California) earthquake, *J. Geophys. Res.*, *109*, B03307, doi:10.1029/2003JB002756.
Fialko, Y. (2006), Interseismic strain accumulation and the earthquake potential on the southern San Andreas fault system, *Nature*, *441*(7096), 968–971, doi:10.1038/nature04797.
Field, E. H., et al. (2014), Uniform California Earthquake Rupture Forecast, Version 3 (UCERF3)—The time-independent model, *Bull. Seismol. Soc. Am.*, *104*(3), 1122–1180, doi:10.1785/0120130164.
Fletcher, J. M., et al. (2014), Assembly of a large earthquake from a complex fault system: Surface rupture kinematics of the 4 April 2010 El Mayor-Cucapah (Mexico) M_w 7.2 earthquake, *Geosphere*, *10*(4), 797–827, doi:10.1130/GES00933.1.
Hadley, D., and H. Kanamori (1977), Seismic structure of the Transverse Ranges, California, *Geol. Soc. Am. Bull.*, *88*(10), 1469–1478.
Hanks, T. C. (1982), f_{max}, *Bull. Seismol. Soc. Am.*, *72*(6A), 1867–1879.
Hardebeck, J. L., J. J. Nazareth, and E. Hauksson (1998), The static stress change triggering model: Constraints from two Southern California aftershock sequences, *J. Geophys. Res.*, *103*(B10), 24,427–24,437, doi:10.1029/98JB00573.
Haskell, N. A. (1969), Elastic displacements in the near-field of a propagating fault, *Bull. Seismol. Soc. Am.*, *59*(2), 865–908.
Hauksson, E. (1994), State of stress from focal mechanisms before and after the 1992 Landers earthquake sequence, *Bull. Seismol. Soc. Am.*, *84*(3), 917–934.
Hauksson, E., L. M. Jones, K. Hutton, and D. Eberhart-Phillips (1993), The 1992 Landers earthquake sequence: Seismological observations, *J. Geophys. Res.*, *98*(B11), 19,835–19,858, doi:10.1029/93JB02384.
Hauksson, E., J. Stock, K. Hutton, W. Yang, J. A. Vidal-Villegas, and H. Kanamori (2011), The 2010 M_w 7.2 El Mayor-Cucapah Earthquake Sequence, Baja California, Mexico and Southernmost California, USA: Active Seismotectonics along the Mexican Pacific Margin, *Pure Appl. Geophys.*, *168*(8–9), 1255–1277, doi:10.1007/s00024-010-0209-7.
Hauksson, E., W. Yang, and P. M. Shearer (2012), Waveform relocated earthquake catalog for Southern California (1981 to June 2011), *Bull. Seismol. Soc. Am.*, *102*(5), 2239–2244, doi:10.1785/0120120010.
Hough, S. E. (1996), Observational constraints on earthquake source scaling: Understanding the limits in resolution, *Tectonophysics*, *261*(1), 83–95, doi:10.1016/0040-1951(96)00058-3.
Hough, S. E. (1997), Empirical Green's function analysis: Taking the next step, *J. Geophys. Res.*, *102*(B3), 5369–5384, doi:10.1029/96JB03488.
Huang, Y., G. C. Beroza, and W. L. Ellsworth (2016), Stress drop estimates of potentially induced earthquakes in the Guy-Greenbrier sequence, *J. Geophys. Res. Solid Earth*, *121*, 6597–6607, doi:10.1002/2016JB013067.
Hutton, K., J. Woessner, and E. Hauksson (2010), Earthquake monitoring in Southern California for seventy-seven years (1932–2008), *Bull. Seismol. Soc. Am.*, *100*(2), 423–446, doi:10.1785/0120090130.
Ide, S. (2003), Apparent break in earthquake scaling due to path and site effects on deep borehole recordings, *J. Geophys. Res.*, *108*(B5), 2271, doi:10.1029/2001JB001617.
Ide, S., and G. C. Beroza (2001), Does apparent stress vary with earthquake size?, *Geophys. Res. Lett.*, *28*(17), 3349–3352, doi:10.1029/2001GL013106.
Izutani, Y., and H. Kanamori (2001), Scale-dependence of seismic energy-to-moment ratio for strike-slip earthquakes in Japan, *Geophys. Res. Lett.*, *28*(20), 4007–4010, doi:10.1029/2001GL013402.
Jiang, J., and Y. Fialko (2016), Reconciling seismicity and geodetic locking depths on the Anza section of the San Jacinto fault, *Geophys. Res. Lett.*, *43*, 10,663–10,671, doi:10.1002/2016GL071113.
Joyner, W. B. (1984), A scaling law for the spectra of large earthquakes, *Bull. Seismol. Soc. Am.*, *74*(4), 1167–1188.
Kagan, Y. Y., D. D. Jackson, and Y. Rong (2006), A new catalog of Southern California earthquakes, 1800–2005, *Seismol. Res. Lett.*, *77*(1), 30–38, doi:10.1785/gssrl.77.1.30.
Kanamori, H., and L. Rivera (2004), Static and dynamic scaling relations for earthquakes and their implications for rupture speed and stress drop, *Bull. Seismol. Soc. Am.*, *94*(1), 314–319, doi:10.1785/0120030159.
Kane, D. L., G. A. Prieto, F. L. Vernon, and P. M. Shearer (2011), Quantifying seismic source parameter uncertainties, *Bull. Seismol. Soc. Am.*, *101*(2), 535–543, doi:10.1785/0120100166.
Kaneko, Y., and P. M. Shearer (2014), Seismic source spectra and estimated stress drop derived from cohesive-zone models of circular subshear rupture, *Geophys. J. Int.*, *197*(2), 1002–1015, doi:10.1093/gji/ggu030.
King, G. C. P., R. S. Stein, and J. Lin (1994), Static stress changes and the triggering of earthquakes, *Bull. Seismol. Soc. Am.*, *84*(3), 935–953.
Kroll, K. A., E. S. Cochran, K. B. Richards-Dinger, and D. F. Sumy (2013), Aftershocks of the 2010 M_w 7.2 El Mayor-Cucapah earthquake reveal complex faulting in the Yuha Desert, California, *J. Geophys. Res. Solid Earth*, *118*, 6146–6164, doi:10.1002/2013JB010529.
Lewis, M. A., Z. Peng, Y. Ben-Zion, and F. L. Vernon (2005), Shallow seismic trapping structure in the San Jacinto fault zone near Anza, California, *Geophys. J. Int.*, *162*(3), 867–881, doi:10.1111/j.1365-246X.2005.02684.x.
Li, Y.-G., and F. L. Vernon (2001), Characterization of the San Jacinto fault zone near Anza, California, by fault zone trapped waves, *J. Geophys. Res. Solid Earth*, *106*(B12), 30,671–30,688, doi:10.1029/2000JB000107.
Lin, J., and R. S. Stein (2004), Stress triggering in thrust and subduction earthquakes and stress interaction between the Southern San Andreas and nearby thrust and strike-slip faults, *J. Geophys. Res.*, *109*, B02303, doi:10.1029/2003JB002607.
Lin, Y.-Y., K.-F. Ma, H. Kanamori, T.-R. A. Song, N. Lapusta, and V. C. Tsai (2016), Evidence for non-self-similarity of microearthquakes recorded at a Taiwan borehole seismometer array, *Geophys. J. Int.*, *206*(2), 757–773, doi:10.1093/gji/ggw172.

Lindsey, E. O., V. J. Sahakian, Y. Fialko, Y. Bock, S. Barbot, and T. K. Rockwell (2014), Interseismic strain localization in the San Jacinto fault zone, *Pure Appl. Geophys.*, *171*(11), 2937–2954, doi:10.1007/s00024-013-0753-z.

Luco, J. E. (1985), On strong ground motion estimates based on models of the radiated spectrum, *Bull. Seismol. Soc. Am.*, *75*(3), 641–649.

Madariaga, R. (1976), Dynamics of an expanding circular fault, *Bull. Seismol. Soc. Am.*, *66*(3), 639–666.

Madariaga, R., J. P. Ampuero, and M. Adda-Bedia (2006), Seismic radiation from simple models of earthquakes, in *Earthquakes: Radiated Energy and the Physics of Faulting*, edited by R. Madariaga, J. P. Ampuero, and M. Adda-Bedia, pp. 223–236, AGU, Washington, D. C.

Mai, P. M., and K. K. S. Thingbaijam (2014), SRCMOD: An online database of finite-fault rupture models, *Seismol. Res. Lett.*, *85*(6), 1348–1357, doi:10.1785/0220140077.

Mayeda, K., and W. R. Walter (1996), Moment, energy, stress drop, and source spectra of western United States earthquakes from regional coda envelopes, *J. Geophys. Res.*, *101*(B5), 11,195–11,208, doi:10.1029/96JB00112.

Mayeda, K., R. Gök, W. R. Walter, and A. Hofstetter (2005), Evidence for non-constant energy/moment scaling from coda-derived source spectra, *Geophys. Res. Lett.*, *32*, L10306, doi:10.1029/2005GL022405.

Mayeda, K., L. Malagnini, and W. R. Walter (2007), A new spectral ratio method using narrow band coda envelopes: Evidence for non-self-similarity in the Hector Mine sequence, *Geophys. Res. Lett.*, *34*, L11303, doi:10.1029/2007GL030041.

Mori, J., and A. Frankel (1990), Source parameters for small events associated with the 1986 North Palm Springs, California, earthquake determined using empirical Green functions, *Bull. Seismol. Soc. Am.*, *80*(2), 278–295.

Mori, J., R. E. Abercrombie, and H. Kanamori (2003), Stress drops and radiated energies of aftershocks of the 1994 Northridge, California, earthquake, *J. Geophys. Res.*, *108*(B11), 2545, doi:10.1029/2001JB000474.

Munafò, I., L. Malagnini, and L. Chiaraluce (2016), On the relationship between M_w and M_L for small earthquakes, *Bull. Seismol. Soc. Am.*, *106*(5), 2402–2408, doi:10.1785/0120160130.

Oth, A. (2013), On the characteristics of earthquake stress release variations in Japan, *Earth Planet. Sci. Lett.*, *377-378*, 132–141, doi:10.1016/j.epsl.2013.06.037.

Oth, A., D. Bindi, S. Parolai, and D. Di Giacomo (2011), Spectral analysis of K-NET and KiK-net data in Japan: Part II. On attenuation characteristics, source spectra, and site response of borehole and surface stations, *Bull. Seismol. Soc. Am.*, *101*(2), 667–687, doi:10.1785/0120100135.

Pacor, F., D. Spallarossa, A. Oth, L. Luzi, R. Puglia, L. Cantore, A. Mercuri, M. D'Amico, and D. Bindi (2016a), Spectral models for ground motion prediction in the L'Aquila region (Central Italy): Evidence for stress-drop dependence on magnitude and depth, *Geophys. J. Int.*, *204*(2), 697–718, doi:10.1093/gji/ggv448.

Pacor, F., F. Gallovič, R. Puglia, L. Luzi, and M. D'Amico (2016b), Diminishing high-frequency directivity due to a source effect: Empirical evidence from small earthquakes in the Abruzzo region, Italy, *Geophys. Res. Lett.*, *43*, 5000–5008, doi:10.1002/2016GL068546.

Papageorgiou, A. S., and K. Aki (1983), A specific barrier model for the quantitative description of inhomogeneous faulting and the prediction of strong ground motion: Part II. Applications of the model, *Bull. Seismol. Soc. Am.*, *73*(4), 953–978.

Park, J., C. R. Lindberg, and F. L. Vernon (1987), Multitaper spectral analysis of high-frequency seismograms, *J. Geophys. Res.*, *92*(B12), 12,675–12,684, doi:10.1029/JB092iB12p12675.

Petersen, M. D., C. S. Mueller, M. P. Moschetti, S. M. Hoover, A. L. Llenos, W. L. Ellsworth, A. J. Michael, J. L. Rubinstein, A. F. McGarr, and K. S. Rukstales (2016), Seismic-hazard forecast for 2016 including induced and natural earthquakes in the Central and Eastern United States, *Seismol. Res. Lett.*, *87*(6), 1327–1341, doi:10.1785/0220160072.

Poli, P., and G. A. Prieto (2016), Global rupture parameters for deep and intermediate-depth earthquakes, *J. Geophys. Res. Solid Earth*, *121*, 8871–8887, doi:10.1002/2016JB013521.

Prieto, G., R. Parker, and F. Vernon III (2009), A Fortran 90 library for multitaper spectrum analysis, *Comput. Geosci.*, *35*(8), 1701–1710, doi:10.1016/j.cageo.2008.06.007.

Prieto, G. A., P. M. Shearer, F. L. Vernon, and D. Kilb (2004), Earthquake source scaling and self-similarity estimation from stacking *P* and *S* spectra, *J. Geophys. Res.*, *109*, B08310, doi:10.1029/2004JB003084.

Prieto, G. A., R. L. Parker, F. L. Vernon, P. M. Shearer, and D. J. Thomson (2006), Uncertainties in earthquake source spectrum estimation using empirical Green functions, in *Geophysical Monograph Series*, vol. 170, edited by R. Abercrombie et al., pp. 69–74, AGU, Washington, D. C.

Prieto, G. A., D. J. Thomson, F. L. Vernon, P. M. Shearer, and R. L. Parker (2007), Confidence intervals for earthquake source parameters, *Geophys. J. Int.*, *168*(3), 1227–1234, doi:10.1111/j.1365-246X.2006.03257.x.

Rockwell, T., C. Loughman, and P. Merifield (1990), Late Quaternary rate of slip along the San Jacinto Fault Zone near Anza, Southern California, *J. Geophys. Res.*, *95*(B6), 8593–8605, doi:10.1029/JB095iB06p08593.

Rockwell, T. K., T. E. Dawson, J. Y. Ben-Horin, and G. Seitz (2015), A 21-event, 4,000-year history of surface ruptures in the Anza seismic gap, San Jacinto Fault, and implications for long-term earthquake production on a major plate boundary fault, *Pure Appl. Geophys.*, *172*(5), 1143–1165, doi:10.1007/s00024-014-0955-z.

Ross, Z. E., and Y. Ben-Zion (2015), An algorithm for automated identification of fault zone trapped waves, *Geophys. J. Int.*, *202*(2), 933–942, doi:10.1093/gji/ggv197.

Ross, Z. E., and Y. Ben-Zion (2016), Toward reliable automated estimates of earthquake source properties from body wave spectra, *J. Geophys. Res. Solid Earth*, *121*, 4390–4407, doi:10.1002/2016JB013003.

Ross, Z. E., E. Hauksson, and Y. Ben-Zion (2017), Abundant off-fault seismicity and orthogonal structures in the San Jacinto fault zone, *Sci. Adv.*, *3*(3), doi:10.1126/sciadv.1601946.

Ross, Z. E., Y. Ben-Zion, M. C. White, and F. L. Vernon (2016), Analysis of earthquake body wave spectra for potency and magnitude values: Implications for magnitude scaling relations, *Geophys. J. Int.*, *207*(2), 1158–1164, doi:10.1093/gji/ggw327.

Sanders, C., H. Magistrale, and H. Kanamori (1986), Rupture patterns and preshocks of large earthquakes in the southern San Jacinto fault zone, *Bull. Seismol. Soc. Am.*, *76*(5), 1187–1206.

Sanders, C. O., and H. Kanamori (1984), A seismotectonic analysis of the Anza Seismic Gap, San Jacinto Fault Zone, Southern California, *J. Geophys. Res. Solid Earth*, *89*(B7), 5873–5890, doi:10.1029/JB089iB07p05873.

Shearer, P. M., G. A. Prieto, and E. Hauksson (2006), Comprehensive analysis of earthquake source spectra in Southern California, *J. Geophys. Res.*, *111*, B06303, doi:10.1029/2005JB003979.

Takahashi, T., H. Sato, M. Ohtake, and K. Obara (2005), Scale dependence of apparent stress for earthquakes along the subducting Pacific plate in Northeastern Honshu, Japan, *Bull. Seismol. Soc. Am.*, *95*(4), 1334–1345, doi:10.1785/0120040075.

Trugman, D. T., and E. M. Dunham (2014), A 2D pseudodynamic rupture model generator for earthquakes on geometrically complex faults, *Bull. Seismol. Soc. Am.*, *104*(1), 95–112, doi:10.1785/0120130138.

Uchide, T., and K. Imanishi (2016), Small earthquakes deviate from the omega-square model as revealed by multiple spectral ratio analysis, *Bull. Seismol. Soc. Am.*, *106*, 1357–1363, doi:10.1785/0120150322.

Uchide, T., P. M. Shearer, and K. Imanishi (2014), Stress drop variations among small earthquakes before the 2011 Tohoku-oki, Japan, earthquake and implications for the main shock, *J. Geophys. Res. Solid Earth*, *119*, 7164–7174, doi:10.1002/2014JB010943.

VanWormer, J. D., and A. S. Ryall (1980), Sierra Nevada-Great Basin boundary zone: Earthquake hazard related to structure, active tectonic processes, and anomalous patterns of earthquake occurrence, *Bull. Seismol. Soc. Am.*, *70*(5), 1557–1572.

Venkataraman, A., G. C. Beroza, S. Ide, K. Imanishi, H. Ito, and Y. Iio (2006), Measurements of spectral similarity for microearthquakes in western Nagano, Japan, *J. Geophys. Res.*, *111*, B03303, doi:10.1029/2005JB003834.

Wald, D. J., and T. H. Heaton (1994), Spatial and temporal distribution of slip for the 1992 Landers, California, earthquake, *Bull. Seismol. Soc. Am.*, *84*(3), 668–691.

Walter, W. R., and J. N. Brune (1993), Spectra of seismic radiation from a tensile crack, *J. Geophys. Res.*, *98*(B3), 4449–4459, doi:10.1029/92JB02414.

Walter, W. R., K. Mayeda, R. Gok, and A. Hofstetter (2006), The scaling of seismic energy with moment: Simple models compared with observations, in *Earthquakes: Radiated Energy and the Physics of Faulting*, edited by W. R. Walter et al., pp. 25–41, AGU, Washington, D. C.

Wdowinski, S. (2009), Deep creep as a cause for the excess seismicity along the San Jacinto fault, *Nat. Geosci.*, *2*(12), 882–885, doi:10.1038/ngeo684.

Wei, S., et al. (2011), Superficial simplicity of the 2010 El Mayor-Cucapah earthquake of Baja California in Mexico, *Nat. Geosci.*, *4*(9), 615–618, doi:10.1038/ngeo1213.

Wesnousky, S. G., J. M. Bormann, C. Kreemer, W. C. Hammond, and J. N. Brune (2012), Neotectonics, geodesy, and seismic hazard in the Northern Walker Lane of Western North America: Thirty kilometers of crustal shear and no strike-slip?, *Earth Planet. Sci. Lett.*, *329-330*, 133–140, doi:10.1016/j.epsl.2012.02.018.

Yang, W., and Y. Ben-Zion (2010), An algorithm for detecting clipped waveforms and suggested correction procedures, *Seismol. Res. Lett.*, *81*(1), 53–62, doi:10.1785/gssrl.81.1.53.

Yenier, E., and G. M. Atkinson (2014), Equivalent point source modeling of moderate to large magnitude earthquakes and associated ground motion saturation effects, *Bull. Seismol. Soc. Am.*, doi:10.1785/0120130147.

Yenier, E., and G. M. Atkinson (2015), Regionally adjustable generic ground motion prediction equation based on equivalent point source simulations: Application to Central and Eastern North America, *Bull. Seismol. Soc. Am.*, *105*(4), 1989–2009, doi:10.1785/0120140332.

Zöller, G., and Y. Ben-Zion (2014), Large earthquake hazard of the San Jacinto Fault zone, CA, from long record of simulated seismicity assimilating the available instrumental and paleoseismic data, *Pure Appl. Geophys.*, *171*(11), 2955–2965, doi:10.1007/s00024-014-0783-1.